AD-A262 273

MASSACHUSETTS INSTITUTE OF TECHNOLOGY
LINCOLN LABORATORY

SOLID STATE RESEARCH

QUARTERLY TECHNICAL REPORT

1 MAY — 31 JULY 1992

ISSUED 31 JANUARY 1993

93-06218

LEXINGTON   MASSACHUSETTS

This technical report has been reviewed and is approved for publication.

FOR THE COMMANDER

Gary Dutungian
Administrative Contracting Officer
Directorate of Contracted Support Management

MASSACHUSETTS INSTITUTE OF TECHNOLOGY
LINCOLN LABORATORY

SOLID STATE RESEARCH

QUARTERLY TECHNICAL REPORT

1 MAY — 31 JULY 1992

ISSUED 31 JANUARY 1993

LEXINGTON   MASSACHUSETTS

ABSTRACT

This report covers in detail the research work of the Solid State Division at Lincoln Laboratory for the period 1 May through 31 July 1992. The topics covered are Electrooptical Devices, Quantum Electronics, Materials Research, Submicrometer Technology, High Speed Electronics, Microelectronics, and Analog Device Technology. Funding is provided primarily by the Air Force, with additional support provided by the Army, DARPA, Navy, SDIO, and NASA.

Accesion For		
NTIS CRA&I		X
DTIC TAB		☐
Unannounced		☐
Justification		
By		
Distribution /		
Availability Codes		
Dist	Avail and / or Special	
A-1		

DTIC QUALITY INSPECTED 1

TABLE OF CONTENTS

LIST OF ILLUSTRATIONS

LIST OF ILLUSTRATIONS (Continued)

LIST OF ILLUSTRATIONS (Continued)

ix

LIST OF ILLUSTRATIONS (Continued)

LIST OF TABLES

INTRODUCTION

1. ELECTROOPTICAL DEVICES

Effective phosphorus vapor concentration in an annealing furnace with PH_3 flow has been modeled analytically, and its definitive relationship with gas-flow velocity and furnace length has been derived. A simple system design guide is presented for achieving a reproducible maximum concentration.

Optical damage (photorefractive) effects have been evaluated in both Ti-indiffused and proton-exchanged waveguides in lithium niobate using power levels up to 400 mW and times up to 200 h. Low-temperature anneals in dry nitrogen were found to substantially increase damage effects.

Linear arrays of InGaAs/AlGaAs ridge waveguide lasers have been fabricated using ion-beam-assisted etching. A 30-element array of uncoated 2-μm-wide, 200-μm-long ridge waveguide lasers exhibited good uniformity, with threshold currents and differential quantum efficiencies that averaged 4.2 mA and 46% per facet, respectively.

2. QUANTUM ELECTRONICS

A CW-pumped, repetitively Q-switched, InGaAs-diode-pumped Yb:YAG laser has been demonstrated at room temperature. An output energy up to 72 μJ/pulse at 1.03 μm, with a pulse length as short as 11 ns (full width at half-maximum), was attained.

3. MATERIALS RESEARCH

Double-crystal x-ray diffraction has been shown to reveal the onset of relaxation in strained-layer InGaAs/GaAs multiple quantum well (MQW) structures. Critical layer thicknesses for thick-barrier InGaAs/GaAs MQW structures were found consistent with the Matthews and Blakeslee force-balance model with dislocation formation by the single-kink mechanism.

Normal-incidence intersubband infrared absorption in n-type quantum wells made from III V materials has been observed for the first time. Consistent with previous theoretical calculations, the absorption occurs in indirect-bandgap (100) $Al_{0.09}Ga_{0.91}Sb$ quantum wells and peaks at wavelengths of 9.5 and 11.5 μm for 6.4- and 7.0-μm-thick quantum wells, respectively.

4. SUBMICROMETER TECHNOLOGY

A high-contrast resist process using polysilynes has been developed for 193-nm excimer laser lithography. Optimal formulations yield sensitivities of 35 to 60 mJ/cm^2, which can be further improved by the addition of sensitizers, and line-edge roughness of 20 nm.

A model has been developed for positive-tone silylation processing for 193-nm lithography. The silylation profile is predicted from the aerial image, the relationship between silylation depth and exposure dose, and the effect of swelling stress in the polymer film.

5. HIGH SPEED ELECTRONICS

The emission properties of candidate materials for new field-emission cathodes have been evaluated using a scanning tunneling microscope. The realization of RF power tubes having significantly improved efficiency demands that traditional heated thermionic cathodes be replaced by such novel cathode structures that emit electrons at room temperature via field emission.

6. MICROELECTRONICS

A new 1024×1024-pixel frame-transfer charge-coupled device (CCD) imager has been designed and fabricated. Initial yields of this large device have been better than anticipated, and the first test results indicate that the device performs as expected.

The charge-transfer inefficiency (CTI) of CCDs irradiated with high-energy protons has been measured at reduced temperatures as a function of charge packet size. The CTI initially decreases until the channel trough is filled, after which there is an increase in CTI to a local maximum.

7. ANALOG DEVICE TECHNOLOGY

The nonlinear surface impedance $Z_s(H_{rf})$, where H_{rf} is the RF magnetic field, has been measured as a function of temperature and frequency in $YBa_2Cu_3O_{7-x}$ thin films, using a stripline resonator. The behavior of $Z_s(H_{rf})$ is characterized by a low-field region that may be due to weak links, an intermediate field region where $Z_s \propto H_{rf}^2$, and a high-field region where flux penetration probably determines the losses.

REPORTS ON SOLID STATE RESEARCH

1 MAY THROUGH 31 JULY 1992

PUBLICATIONS

20-GHz High-Efficiency Power Amplifiers Using Monolithic Multi-cell Permeable Base Transistors	R. Actis K. B. Nichols R. W. Chick R. A. McMorran	*1992 IEEE MTT-S Int.* *Microwave Symp. Dig.* (IEEE, New York, 1992), Vol. 1, p. 281
High-Breakdown-Voltage MESFET with a Low-Temperature-Grown GaAs Passivation Layer and Overlapping Gate Structure	C. L. Chen L. J. Mahoney M. J. Manfra F. W. Smith D. H. Temme A. R. Calawa	*IEEE Electron Device Lett.* **13**, 335 (1992)
An Externally Modulated Fiber-Optic Link Test Bed for Characterizing Link Performance in a System	C. H. Cox III L. A. Bernotas G. E. Betts A. I. Grayzel D. R. O'Brien J. J. Scozzafava A. C. Yee	*1992 IEEE MTT-S Int.* *Microwave Symp. Dig.* (IEEE, New York, 1992), Vol. 2, p. 575
Device Quality Diamond Substrates	M. W. Geis	In *Diamond, Diamond-Like and Related Coatings 1991*, P. K. Bachman and A. Matthews, eds. (Elsevier, Amsterdam, 1992), p. 684
Superconductive Analog Electronics for Signal Processing Applications	J. B. Green	*NATO Advanced Research Workshop on Nonlinear Superconductive Electronics: Nonlinear Superconductive Electronics and Josephson Devices* (Plenum, New York, 1991), p. 119

Very High Efficiency GaInAsP/GaAs Strained-Layer Quantum Well Lasers (λ = 980 nm) with GaInAsP Optical Confinement Layers	S. H. Groves J. N. Walpole L. J. Missaggia	*Appl. Phys. Lett.* **61**, 255 (1992)
Sub-0.25 Micrometer 193 nm Optical Lithography	M. A. Hartney M. W. Horn R. R. Kunz M. Rothschild D. C. Shaver	*Microlithogr. World* **1**, 6 (1992)
Silylation Process for 193-nm Lithography Using Acid Catalyzed Resists	M. A. Hartney J. W. Thackeray*	*Proc. SPIE* **1672**, 486 (1992)
A Comparison of Etching Tools for Resist Pattern Transfer	M. W. Horn M. A. Hartney R. R. Kunz	*Proc. SPIE* **1672**, 448 (1992)
Time and Temperature Dependence of Phosphorus Vapor Pressure As Measured by a Pressure-Balanced, Sealed-Ampoule Technique	G. W. Iseler H. R. Clark, Jr. D. F. Bliss*	*Proc. Fourth Int. Conf. on Indium Phosphide and Related Compounds* (IEEE, New York, 1992), p. 266
Phase Locking of 1.32-μm Microchip Lasers Through the Use of Pump-Diode Modulation	J. A. Keszenheimer E. J. Balboni* J. J. Zayhowski	*Opt. Lett.* **17**, 649 (1992)
Selective-Area Growth of Metal Oxide Films Induced by Patterned Excimer Laser Surface Photolysis	R. R. Kunz D. J. Ehrlich J. Melngailis M. W. Horn	*Proc. Mater. Res. Soc. Symp.* **236**, 105 (1992)
Surface-Imaged Silicon Polymers for 193-nm Excimer Laser Lithography	R. R. Kunz M. W. Horn R. B. Goodman G. M. Wallraff* R. D. Miller* P. A. Bianconi*	*Proc. SPIE* **1672**, 385 (1992)

---

*Author not at Lincoln Laboratory.

Modeling the Nonlinearity of Superconducting Strip Transmission Lines	C.-W. Lam* D. M. Sheen* S. M. Ali* D. E. Oates	*IEEE Trans. Appl. Superconduct.* **2**, 58 (1992)
Nonlinear Model of Superconducting Strip Transmission Lines	C. W. Lam* D. M. Sheen* S. M. Ali* D. E. Oates	*1992 IEEE MTT-S Int. Microwave Symp. Dig.* (IEEE, New York, 1992), Vol. 1, p. 197
Full-Wave Characterization of High-T_c Superconducting Transmission Lines	L. H. Lee* S. M. Ali* W. G. Lyons	*IEEE Trans. Appl. Superconduct.* **2**, 49 (1992)
Laser Induced Damage in Pellicles at 193 nm	M. Rothschild J. H. C. Sedlacek	*Proc. SPIE* **1674**, 618 (1992)
A Small-Field Stepper for 193-nm Lithography Process Development	D. C. Shaver D. M. Craig C. A. Marchi M. A. Hartney F. Goodall*	*Proc. SPIE* **1674**, 766 (1992)
Optical Interconnections for Digital Systems	D. Z. Tsang	*Proc. 1992 National Telesystems Conf.* (IEEE, New York, 1992), p. 9-1

ACCEPTED FOR PUBLICATION

High-Speed Resonant-Tunneling Diodes	E. R. Brown	In *Heterostructure and Quantum Devices* (Academic, Orlando, Fla.)
Observation of Normal-Incidence Intersubband Absorption in n-AlGaSb Quantum Wells	E. R. Brown S. J. Eglash K. A. McIntosh	*Phys. Rev. Lett.*

---

*Author not at Lincoln Laboratory.

Strong Intersubband Absorption by Photogenerated Carriers in Quantum Wells	E. R. Brown K. A. McIntosh K. B. Nichols	*Proc. SPIE*
A Quasioptical Resonant-Tunneling Diode Oscillator Operating Above 200 GHz	E. R. Brown C. D. Parker A. R. Calawa M. J. Manfra K. M. Molvar	*IEEE Trans. Microwave Theory Tech.*
Radiation Properties of a Planar Antenna on a Photonic Crystal Substrate	E. R. Brown C. D. Parker E. Yablonovitch*	*J. Opt. Soc. Am. B*
Coherent Millimeter-Wave Generation by Heterodyne Conversion in Low-Temperature-Grown GaAs Photoconductors	E. R. Brown F. W. Smith K. A. McIntosh	*Appl. Phys. Lett.*
Analysis of Heterojunction Bipolar Transistor/Resonant-Tunneling-Diode Logic for Low-Power and High-Speed Digital Applications	C. E. Chang* P. M. Asbeck* K. C. Wang* E. R. Brown	*IEEE Trans. Electron Devices*
High-Power Multiple-Quantum-Well GaInAsSb/AlGaAsSb Diode Lasers Emitting at 2.1 μm with Low Threshold Current Density	H. K. Choi S. J. Eglash	*Appl. Phys. Lett.*
Analog Fiber-Optic Links with Intrinsic Gain	C. H. Cox III	*Microwave J.*
High Quantum Efficiency Monolithic Arrays of Surface-Emitting AlGaAs Diode Lasers with Dry-Etched Vertical Facets and Parabolic Deflecting Mirrors	J. P. Donnelly W. D. Goodhue R. J. Bailey G. A. Lincoln C. A. Wang G. D. Johnson	*Appl. Phys. Lett.*

---

*Author not at Lincoln Laboratory.

Ultralow Dielectric Constant Thick Film Polymer Foams for Advanced Electronic Packaging	P. Ehrlich* D. J. Ehrlich	*Adv. Mater. Opt. Electron.*
Optimizing the Efficiency and Stored Energy in Quasi-Three-Level Lasers	T. Y. Fan	*IEEE J. Quantum Electron.*
An Ionic Liquid-Channel Field-Effect Transistor	S. A. Gajar M. W. Geis	*J. Electrochem. Soc.*
Diamond and Diamondlike Carbon	M. W. Geis	In *Encyclopedia of Applied Physics* (VCH Publishers, New York)
Diamond for Electrical Applications	M. W. Geis J. C. Angus*	*Sci. Am.*
InGaAs/GaInAsP/GaInP Strained-Layer Quantum Well Separate-Confinement Heterostructures Grown by OMVPE	S. H. Groves	*J. Cryst. Growth*
Observation of Optical Pumping of Mesospheric Sodium	T. H. Jeys R. M. Heinrichs K. F. Wall J. Korn T. C. Hotaling E. Kibblewhite*	*Opt. Lett.*
Ultrafast, Multi-THz-Detuning, Third-Order Frequency Conversion in Semiconductor Quantum-Well Waveguides	H. Q. Le S. DiCecca	*IEEE Photon. Technol. Lett.*
5 mW Parallel-Connected Resonant-Tunnelling Diode Oscillator	K. D. Stephan* E. R. Brown S.-C. Wong* K. M. Molvar A. R. Calawa M. J. Manfra	*Electron. Lett.*

---

*Author not at Lincoln Laboratory.

A Ti:Al$_2$O$_3$ Master-Oscillator/Power-Amplifier System	K. F. Wall P. A. Schulz R. L. Aggarwal P. Lacovara A. Sanchez	*IEEE J. Quantum Electron.*
High-Power Strained-Layer InGaAs/AlGaAs Tapered Traveling Wave Amplifier	J. N. Walpole E. S. Kintzer S. R. Chinn C. A. Wang L. J. Missaggia	*Appl. Phys. Lett.*
Radiative Substrate Heating for High T_c Superconducting Thin-Film Deposition: Film-Growth-Induced Temperature Variation	A. C. Westerheim B. I. Choi* R. L. Slattery M. I. Flik* M. J. Cima* A. C. Anderson	*J. Vac. Sci. Technol. A*
A High Flux Atomic Oxygen Source for the Deposition of High T_c Superconducting Films	L. S. Yu-Jahnes W. T. Brogan A. C. Anderson M. J. Cima*	*Rev. Sci. Instrum.*
Diode-Pumped Microchip Lasers Electro-optically Q Switched at High Pulse Repetition Rates	J. J. Zayhowski C. Dill III	*Opt. Lett.*

*Author not at Lincoln Laboratory.

PRESENTATIONS[†]

Resonant-Tunneling-Diode Circuits	T. C. L. G. Sollner	Electrical Engineering Department Seminar, Yale University, New Haven, Connecticut, 1 May 1992
Sub-0.5-μm Patterning Using 193-nm Optical Lithography	D. C. Shaver	VLSI Seminar, Massachusetts Institute of Technology, Cambridge, Massachusetts, 5 May 1992
GaInAsSb/AlGaAsSb Double-Heterostructure and Very-Low-Threshold QW Diode Lasers	H. K. Choi S. J. Eglash	
Monolithic 2-D Surface-Emitting Arrays of AlGaAs Horizontal-Cavity Diode Lasers with Etched Facets and External Parabolic Deflecting Mirrors	J. P. Donnelly R. J. Bailey W. D. Goodhue C. A. Wang G. A. Lincoln G. D. Johnson	
5-GHz Mode-Locking of a Nd:YLF Laser	S. R. Henion P. A. Schulz	1992 Conference on Lasers and Electro-Optics, Anaheim, California, 10-15 May 1992
Yb:YAG Laser: Mode-Locking and High-Power Operation	S. R. Henion P. A. Schulz	
High-Power High-Efficiency cw Nd:Glass Laser	J. Korn T. Y. Fan	
Q-Switched Yb:YAG Lasers	P. Lacovara T. Y. Fan S. Klunk* G. Henein*	

---

*Author not at Lincoln Laboratory.

[†]Titles of presentations are listed for information only. No copies are available for distribution.

Three-Wavelength Interconversion Laser	P. A. Schulz T. H. Jeys	
High-Power Strained-Layer Tapered Unstable-Resonator Laser	J. N. Walpole E. S. Kintzer S. R. Chinn C. A. Wang L. J. Missaggia	1992 Conference on Lasers and Electro-Optics, Anaheim, California, 10-15 May 1992
Diode-Pumped Electro-optically Q-Switched Microchip Lasers	J. J. Zayhowski C. Dill III	
High-Speed Resonant-Tunneling Devices and Circuits	T. C. L. G. Sollner	Resonant Tunneling Devices and Applications, University of Maryland, Baltimore, Maryland, 14 May 1992
Diamond Transistors	M. W. Geis	Industrial Liaison Office Symposium on Electronic Materials, Massachusetts Institute of Technology, Cambridge, Massachusetts, 20-21 May 1992
Diode Lasers Based on GaInAsP/GaAs Materials	S. H. Groves	
InGaAs- and AlInGaAs-AlGaAs Strained-Layer Quantum-Well Diode Lasers Grown by Organometallic Vapor Phase Epitaxy	C. A. Wang	
Laser Micromachining of Three-Dimensional Microstructures	T. M. Bloomstein D. J. Ehrlich	IEEE Electron Devices Society, Boston Chapter Meeting, Waltham, Massachusetts, 21 May 1992
Optical Lithography at Feature Sizes of 0.25 μm and Below	M. A. Hartney M. W. Horn R. R. Kunz M. Rothschild D. C. Shaver	Lincoln Laboratory Technical Seminar Series, University of Rochester, Rochester, New York, 22 May 1992

Laser-Chemical Three-Dimensional Writing of Multimaterial Structures for Microelectromechanics	T. Bloomstein D. J. Ehrlich	36th International Symposium on Electron, Ion, and Photon Beams, Orlando, Florida, 26-29 May 1992
Wet-Developed Bilayer Resists for 193-nm Excimer Laser Lithography	R. R. Kunz M. W. Horn P. A. Bianconi* D. A. Smith* J. R. Eshelman*	
Photolithography at 193 nm and Below	M. Rothschild	
±10 nm Feature Size Control of 320 nm Grating	C. L. Dennis K. B. Nichols	JBX 5DII Users Group Meeting, Orlando, Florida, 30 May 1992
High-T_c Superconductive Passive Microwave Device Applications— Commercial and Military	W. G. Lyons	
Wideband Superconductive Electronic-Intelligence Receiver Applications	W. G. Lyons	
High-T_c Superconductive Microwave-Receiver Components	W. G. Lyons R. S. Withers J. D. Goettee* D. E. Oates A. C. Anderson J. S. Herd*	1992 IEEE MTT-S International Microwave Symposium, Albuquerque, New Mexico, 1-5 June 1992
5-mW Parallel Connected Resonant-Tunneling Diode Oscillator	K. D. Stephan* E. R. Brown S.-C. Wong* K. M. Molvar A. R. Calawa M. J. Manfra	

*Author not at Lincoln Laboratory.

Critical Issues for Single-Chamber Manufacturing: The Role of Laser Technology	D. J. Ehrlich	1992 European Materials Research Society Spring Meeting, Strasbourg, France, 2-5 June 1992
Laser Induced Microfabrication Technologies	D. J. Ehrlich	Laser Advanced Materials Processing '92, Nagaoka, Japan, 7-12 June 1992
Optical Lithography at Feature Sizes of 0.25 μm and Below	M. W. Horn M. A. Hartney R. R. Kunz M. Rothschild D. C. Shaver	Plasma Etch Users Group of Northern California Chapter of American Vacuum Society, Palo Alto, California, 11 June 1992
Diamond Schottky Diodes	M. W. Geis	
Diamond Field Emission Cathodes	M. W. Geis J. C. Twichell C. O. Bozler D. D. Rathman S. Rabe J. J. Cuomo*	Gordon Research Conference, Plymouth, New Hampshire, 15-19 June 1992
High-T_c Superconductors at Microwave Frequencies: Fundamental Properties and Applications	D. E. Oates	Seminar, University of Karlsruhe, Karlsruhe, Germany, 19 June 1992
Wide-Bandwidth, High-Sensitivity, Coherent Detection Using GaAs/ AlGaAs MQW Structures	E. R. Brown K. A. McIntosh F. W. Smith M. J. Manfra	Fiftieth Annual Device Research Conference, Cambridge, Massachusetts, 22-24 June 1992
Low-Threshold GaInAsSb/AlGaAsSb Quantum-Well Ridge-Waveguide Lasers Emitting at 2.1 μm	H. K. Choi S. J. Eglash M. K. Connors	

*Author not at Lincoln Laboratory.

An Ionic Liquid-Channel Field-Effect
Transistor

S. A. Gajar
M. W. Geis

Theory and Simulation of Ion-
Implanted Laterally Graded Gunn-
Effect Diodes

C. R. Musil*
H. J. Lezec*
D. A. Antoniadis*
J. Melngailis*
L. J. Mahoney

Fiftieth Annual Device
Research Conference,
Cambridge, Massachusetts,
22-24 June 1992

High-T_c Superconductors at Microwave
Frequencies: Fundamental Properties
and Applications

D. E. Oates

Seminar, University
of Wuppertal,
Karlsruhe, Germany,
23 June 1992

GaInAsSb Quantum Wells and
Metastable Alloys Grown by MBE

S. J. Eglash
H. K. Choi
G. W. Turner
D. R. Calawa

Critical Layer Thickness and
Photoluminescence Properties of
Strained-Layer InGaAs-GaAs
Multiple Quantum Wells

C. A. Wang
S. H. Groves
J. H. Reinold
D. R. Calawa

1992 Electronic Materials
Conference,
Cambridge, Massachusetts,
24-26 June 1992

Comparison of Surface Morphology
and Microstructure of *In Situ* and
Ex Situ Derived $YBa_2Cu_3O_{7-x}$
Thin Films

A. C. Westerheim
P. C. McIntyre*
S. N. Basu*
D. Bhatt*
L. S. Yu-Jahnes
A. C. Anderson
M. J. Cima*

External-Modulator Analog Link
with Optical Amplifier

L. M. Johnson
B. R. Hemenway
H. V. Roussell

Third Topical Meeting on
Optical Amplifiers and
Their Applications,
Santa Fe, New Mexico,
24-26 June 1992

---

*Author not at Lincoln Laboratory.

Integrated Optical Modulators	G. E. Betts	Seminar, Digital Equipment Corporation, Littleton, Massachusetts, 26 June 1992
Diamond Transistors	M. W. Geis	Annual Diamond Conference, London, England, 5-8 July 1992
Diamond Transistors	M. W. Geis	Technical Seminar, Kobe Steel, Surrey, England, 10 July 1992
Diamond Transistors	M. W. Geis	Technical Seminar, Philips Research Laboratories, West Aachen, Germany, 13 July 1992
Surface Imaging Resists for 193-nm Lithography	D. W. Johnson* M. A. Hartney	
Surface-Imaged Silicon Polymers for 193-nm Excimer Laser Lithography	R. R. Kunz M. W. Horn R. B. Goodman G. M. Wallraff* R. D. Miller* P. A. Bianconi*	1992 Microprocess Conference, Kawasaki, Japan, 13-16 July 1992
Diamond Transistors	M. W. Geis	The Royal Society, London, England, 15-16 July 1992

---

*Author not at Lincoln Laboratory.

High Performance Analog Fiber-Optic Links for Antenna Applications	C. H. Cox III	1992 IEEE Antennas and Propagation Society International Symposium, Chicago, Illinois, 18-25 July 1992
Experimental Results on a 12-GHz 16-Element Multilayer Microstrip Array with a High-T_c Superconducting Feed Network	J. S. Herd* J. P. Kenney* K. G. Herd* W. G. Lyons A. C. Anderson P. M. Mankiewich* M. L. O'Malley*	
Microwave Characterization of High-T_c Superconducting Thin Films and Devices	W. G. Lyons D. E. Oates	International Union of Radio Scientists Meeting, Chicago, Illinois, 18-25 July 1992
Polysilyne Resists for 193-nm Excimer Laser Lithography	R. R. Kunz	Technical Seminar, Matshusita, Osaka, Japan, 20 July 1992
Optical Pumping of Mesospheric Sodium: A New Measurement Capability	R. M. Heinrichs T. H. Jeys K. F. Wall J. Korn	16th International Laser Radar Conference, Massachusetts Institute of Technology, Cambridge, Massachusetts, 20-24 July 1992
Development of Mesospheric Sodium Laser Beacon for Atmospheric Adaptive Optics	T. H. Jeys	
Polysilyne Resists for 193-nm Excimer Laser Lithography	R. R. Kunz	Technical Seminar, Hitachi, Kokubunji, Japan, 22 July 1992
Polysilyne Resists for 193-nm Excimer Laser Lithography	R. R. Kunz	Technical Seminar, Fujitsu, Osaka, Japan, 23 July 1992

---

*Author not at Lincoln Laboratory.

Comparison of GaAs/AlGaAs Quantum-Well IR Detectors Fabricated on GaAs and Si Substrates

E. R. Brown
F. W. Smith
G. W. Turner
K. A. McIntosh
M. J. Manfra
C. A. Graves

SPIE Conference on
Advanced Detectors,
San Diego, California,
24 July 1992

Polysilyne Resists for 193-nm Excimer Laser Lithography

R. R. Kunz

Technical Seminar,
Nippon Telephone
and Telegraph,
Atsugi, Japan,
25 July 1992

Steps Toward the Practical Application of Externally Modulated Fiber-Optic Links

C. H. Cox III
L. A. Bernotas
G. E. Betts
D. R. O'Brien
J. J. Scozzafava
A. C. Yee

IEEE Lasers and Electro-Optics
Society Summer Topical
Meetings,
Santa Barbara, California,
29-30 July 1992

ORGANIZATION

SOLID STATE DIVISION

A. L. McWhorter, *Head*
I. Melngailis, *Associate Head*
E. Stern, *Associate Head*
D. C. Shaver, *Assistant Head*
J. F. Goodwin, *Assistant*

D. J. Ehrlich, *Senior Staff*
N. L. DeMeo, Jr., *Associate Staff*
J. W. Caunt, *Assistant Staff*
K. J. Challberg, *Administrative Staff*

SUBMICROMETER TECHNOLOGY

M. Rothschild, *Leader*
T. M. Lyszczarz, *Assistant Leader*

Astolfi, D. K.	Hartney, M. A.
Craig, D. M.	Horn, M. W.
Dennis, C. L.	Keast, C. L.
DiNatale, W. F.	Kunz, R. R.
Doran, S. P.	Maki, P. A.
Efremow, N. N., Jr.	Melngailis, J.[†]
Forte, A. R.	Sedlacek, J. H. C.
Geis, M. W.	Twichell, J. C.
Goodman, R. B.	Uttaro, R. S.
	Hotaling, T. C.

QUANTUM ELECTRONICS

A. Mooradian, *Leader*
P. L. Kelley, *Associate Leader*
A. Sanchez-Rubio, *Assistant Leader*

Aggarwal, R. L.	Hsu, L.*
Cook, C. C.	Jeys, T. H.
Daneu, V.	Korn, J. A.
DeFeo, W. E.	Lacovara, P.
DiCecca, S.	Le, H. Q.
Dill, C. D., III	Nabors, C. D.
Fan, T. Y.	Ochoa, J. R.
Hancock, R. C.	Schulz, P. A.
Henion, S. R.	Sullivan, D. J.
Zayhowski, J. J.	

ELECTRONIC MATERIALS

A. J. Strauss, *Leader*
B-Y. Tsaur, *Associate Leader*

Anderson, C. H., Jr.	Kolesar, D. F.
Button, M. J.	Krohn, L., Jr.
Chen, C. K.	Marino, S. A.
Choi, H. K.	Mastromattei, E. L.
Clark, H. R., Jr.	McGilvary, W. L.
Connors, M. K.	Nitishin, P. M.
Eglash, S. J.	Pantano, J. V.
Fahey, R. E.	Reinold, J. H., Jr.
Finn, M. C.	Turner, G. W.
Iseler, G. W.	Wang, C. A.

HIGH SPEED ELECTRONICS

R. A. Murphy, *Leader*
M. A. Hollis, *Assistant Leader*
R. W. Chick, *Senior Staff*

Actis, R.	Mathews, R. H.
Bozler, C. O.	Mattia, J. P.*
Brown, E. R.	McIntosh, K. A.
Calawa, A. R.	McMorran, R. A.
Chen, C. L.	McNamara, M. J.
Clifton, B. J.[‡]	Nichols, K. B.
Goodhue, W. D.	Parker, C. D.
Harris, C. T.	Rabe, S.
Lincoln, G. A., Jr.	Rathman, D. D.
Mahoney, L. J.	Smith, F. W., III
Manfra, M. J.	Vera, A.

---

* Research Assistant
† Part Time
‡ Leave of Absence

1. ELECTROOPTICAL DEVICES

1.1 ANALYSIS OF PHOSPHORUS VAPOR CONCENTRATION IN AN ANNEALING FURNACE WITH PH_3 FLOW

Phosphorus vapor concentration is a key parameter that unfortunately is not precisely known and controlled in most annealing, processing, and crystal growth of phosphorus-containing III-V compound semiconductors [1]-[5]. In this work, a simple one-dimensional analytical model has been developed for an open-tube furnace system with a known PH_3 concentration C_0 (usually a few percent) in the gas in-flow. We show that the phosphorus vapor concentration in the system can be significantly lowered by diffusion and condensation to cooler regions. Techniques are then proposed for the prevention of this "cold trap" effect, so that a reproducible, known phosphorus vapor concentration can be achieved.

The model is illustrated in Figure 1-1(a). At steady state, the phosphorus vapor concentration $C(x)$ is described by the continuity equation

$$D\frac{d^2C}{dx^2} - v\frac{dC}{dx} + g(x) = 0 \ , \tag{1.1}$$

where D is the vapor diffusivity, v is the gas-flow velocity, and $g(x)$ is the phosphorus-vapor generation due to the PH_3 thermal decomposition. The rate of PH_3 decomposition depends on the furnace temperature, flow velocity, and perhaps also materials used in the furnace tube [3],[4]. With a constant decomposition rate in a given system, PH_3 concentration in the furnace can be expected to follow an exponential decay with a characteristic length ℓ. When ℓ is much smaller than the furnace length L, the in-flow PH_3 is fully decomposed in the furnace. We then have $\int_0^\infty g(x)dx = C_0 v$, which in turn yields

$$g(x) = \frac{C_0 v}{\ell} e^{-x/\ell} \ . \tag{1.2}$$

Note that we make no distinction between different vapor species, P_2 and P_4, and that $C(x)$ represents the total atomic concentration.

Equation (1.1) is a linear differential equation, for which standard methods can readily be applied for homogeneous and particular solutions. The resulting general solution is

$$C(x) = B_1 + B_2 e^{vx/D} - \frac{C_0 \ell}{\ell + \frac{D}{v}} e^{-x/\ell} \ . \tag{1.3}$$

The coefficients B_1 and B_2 are then determined by the boundary conditions $C(0) = C(L) = 0$. (Vapor pressure of condensed phosphorus is negligibly small [6] and forms a constant background throughout the entire system.) Hence,

$$C(x) = \frac{C_0 \ell}{\ell + \frac{D}{v}} \left[1 - e^{-x/\ell} - \left(1 - e^{-L/\ell}\right)\left(e^{vx/D} - 1\right)\left(e^{vL/D} - 1\right)^{-1} \right] \ . \tag{1.4}$$

1

(a)

(b)

(c)
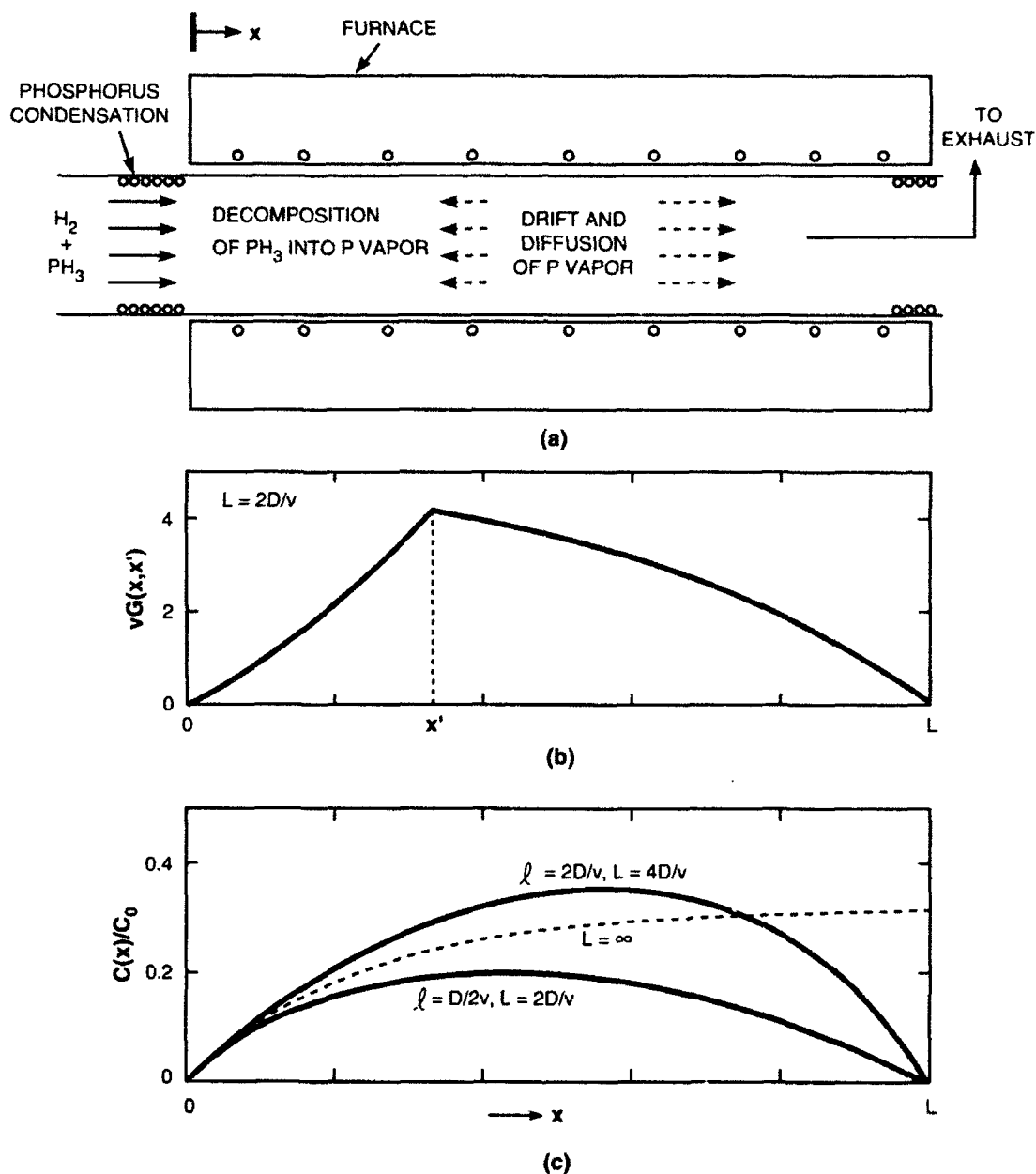
Figure 1-1. (a) Generation, drift, diffusion, and condensation of phosphorus vapor in a furnace system, (b) the phosphorus vapor concentration profile for a point source at x', and (c) total phosphorus concentrations for different drift and diffusion parameters.

2

Alternatively, Equation (1.1) can also be solved by using the Green's function method, which can provide more physical insight and is potentially more applicable to other possible forms of $g(x)$. In this method, the vapor concentration produced by a point source is first considered, i.e.,

$$D\frac{d^2G(x,x')}{dx^2} - v\frac{dG(x,x')}{dx} + \delta(x-x') = 0 \ .$$

(1.5)

The solution to Equation (1.1) is then given by

$$C(x) = \int_0^L G(x,x')g(x')dx' \ .$$

(1.6)

Equation (1.5) easily yields

$$G(x,x') = \begin{cases} C_1 + C_2 e^{vx/D} & \text{for } x \le x' \\ C_3 + C_4 e^{vx/D} & \text{for } x \ge x' \end{cases} .$$

(1.7)

The coefficients C_1 through C_4 are then determined by the boundary conditions:

(i) $G = 0$ at both $x = 0$ and $x = L$,

(ii) G continuous at $x = x'$, and

(iii) $\left[vG - D\frac{dG}{dx}\right]_{x=0}^{x=L} = 1$ (conservation of total flux),

which can readily be solved to yield

$$C_1 = -C_2 = -\frac{1}{v}\left(e^{-vx'/D} - e^{-vL/D}\right)\Big/\left(1 - e^{-vL/D}\right)$$

(1.8a)

$$C_3 = \left(-e^{vL/D}\right)C_4 = \frac{1}{v}\left(1 - e^{-vx'/D}\right)\Big/\left(1 - e^{-vL/D}\right) \ .$$

(1.8b)

The function $G(x,x')$ thus obtained is illustrated in Figure 1-1(b), which indeed reflects the drift, diffusion, and condensation of vapor generated at the point x'.

The total concentration $C(x)$ is then obtained by evaluating Equation (1.6), in which the integration can be carried out analytically to obtain a solution identical to Equation (1.4). Two examples of calculated $C(x)$ are shown in the solid curves in Figure 1-1(c). It can be seen that the maximum concentrations are substantially lower than C_0, which is the concentration expected for a complete PH_3 pyrolysis but without phosphorus diffusion and condensation. The lower concentration is especially true for larger D/v, as expected.

In the case of a long furnace, where $L \to \infty$, Equation (1.4) becomes

$$C(x) = \frac{C_0 \ell}{\ell + \dfrac{D}{v}}\left(1 - e^{-x/\ell}\right) \ ,$$

(1.9)

3
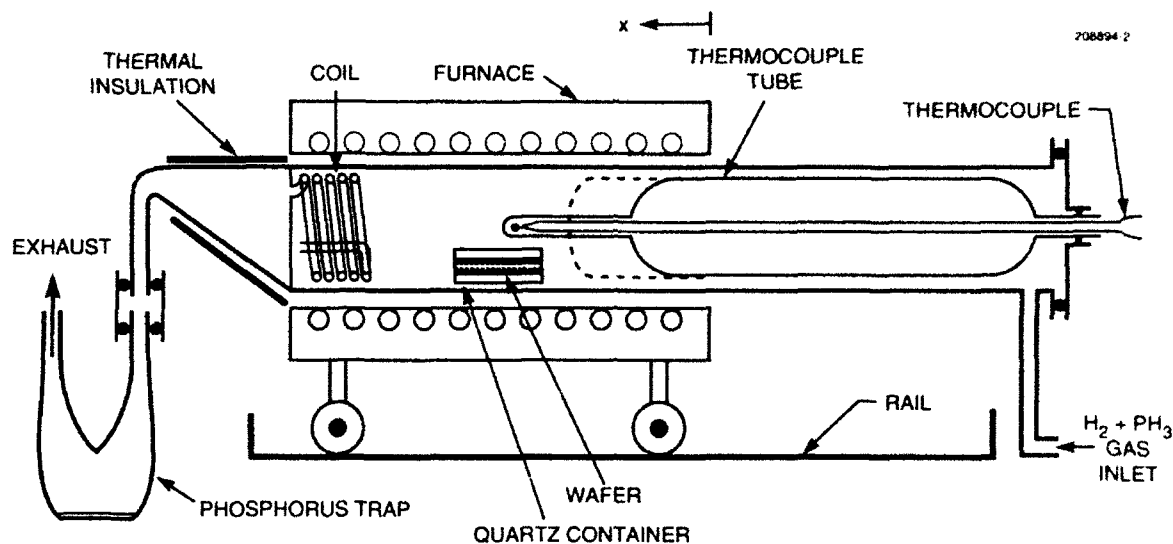
Figure 1-2. Reactor design for maximum phosphorus vapor concentration.

as illustrated in the dashed curve in Figure 1-1(c). Note that $C(x)$ climbs to a saturation value of

$$C_{max} = \frac{C_0 \ell}{\ell + \dfrac{D}{v}} \cdot \tag{1.10}$$

This is larger than the maximum concentration obtained for a finite L, because the additional diffusion loss at $x = L$ now has little effect on the maximum vapor concentration. This long furnace effect can be achieved alternatively by implementing a coiled region, as illustrated in Figure 1-2. (The furnace system is otherwise rather similar to that in [5].)

Equation (1.10) shows that the concentration C_0 can be approached by increasing ℓ or v; note that increased ℓ means generation of phosphorus vapor farther away from the cold front end, and the increased v makes for more difficult outdiffusion. Experimentally, both conditions can be achieved simultaneously by extending the enlarged thermocouple tube, as illustrated by the dashed drawing in Figure 1-2. This enlarged tube decreases the cross-sectional area of the gas flow and hence increases v, which in turn increases ℓ for the same PH_3 decomposition lifetime. The elimination of phosphorus condensation in the front end is also highly desirable for maintaining a clean system.

In conclusion, an analytical model has been developed for a quantitative evaluation of the phosphorus vapor concentration in an annealing furnace. Depending strongly on the gas flow velocity and furnace length, the phosphorus vapor concentration can be far lower than the input PH_3 concentration, because of diffusion and condensation. The present model offers a design guide for achieving maximum, reproducible phosphorus vapor concentration.

Z. L. Liau

4

1.2 MEASUREMENTS OF OPTICAL DAMAGE IN LiNBO$_3$ WAVEGUIDES AT 1320 nm

Optical damage is known to be a problem at short ($\leq$ 830 nm) wavelengths in lithium niobate (LiNbO$_3$) waveguides, but there have been few reports of damage at ~1300 nm [7] because of the higher damage threshold. Possible optical damage to LiNbO$_3$ waveguides at high power at 1300 nm has now become a practical issue, owing to the use of the devices in analog optical links [8]. We report here the results of long-term, high-power tests of LiNbO$_3$ devices made using both Ti-indiffused and proton-exchanged waveguides.

The basic optical damage mechanism is the photorefractive effect, in which illuminated regions experience a refractive index change [9]. This can manifest itself in several ways in an optical waveguide: (1) the optical path length (the total phase shift of the light passing through a given length of waveguide) can change, (2) the waveguide loss can change because the photorefractive index change reduces the waveguide/substrate index difference, (3) TE-polarized light can be converted to TM by an induced index grating [10], and (4) the mode shape can change because of changes in the waveguide index profile. We have observed the first three of these effects in LiNbO$_3$ devices operated at high power at 1320 nm, and there may have been small mode shape or position changes as well.

In an interferometric modulator, illustrated in Figure 1-3, these waveguide changes affect the modulation performance. Different changes in total phase shift in the two arms (due to any slight imbalance in power or damage sensitivity) cause a change in the modulator bias point, which is the relative phase difference between arms. The bias point change is usually the most sensitive measure of damage, but it is a practical problem only in applications that do not actively control the modulator bias point. The on-to-off, or extinction, ratio can be degraded by unbalanced losses in the two arms or unbalanced splitting at the Y-branches due to a photorefractive index change.
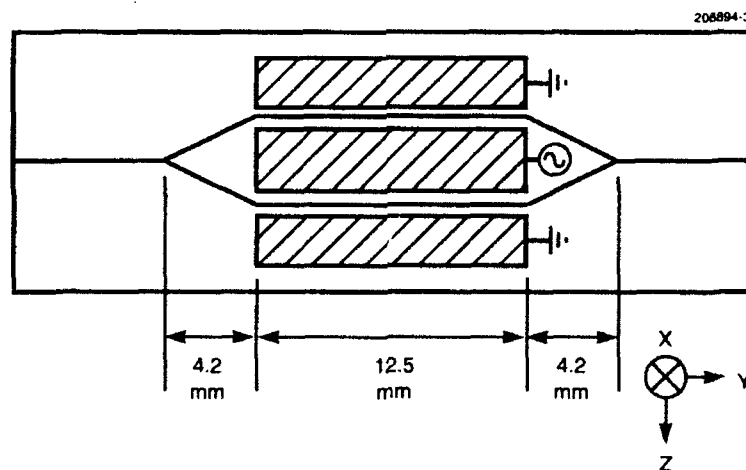
Figure 1-3. Diagram of interferometric modulator.

5

We have evaluated both straight waveguides and interferometric modulators. The majority of devices tested had 6-μm-wide Ti-indiffused waveguides (70-nm Ti; diffusion for 6 h at 1050°C in wet O_2) on optical waveguide substrates. The devices with proton-exchanged (PE) waveguides were exchanged in pure benzoic acid at 215°C, then annealed in wet O_2 at 360°C for various process times. All devices were X-cut and Y-propagating and used the TE polarization. The waveguide losses were < 0.1 dB/cm, for all but one PE sample that had poor guides. The modulators all had a 250-nm-thick SiO_2 buffer layer under the electrodes. The Y-branches in the interferometers had a power balance of 52:48 or better and a loss < 0.2 dB.

For most of our measurements, we used a diode-pumped Nd:YLF laser operating at 1321 nm, which was lens coupled to the test devices. (Fiber coupling does not seem to change the damage characteristics, but so far we have tested fiber-coupled devices only up to 95 mW.) Measurements were made at various optical power levels in the waveguide just after input coupling. Since the losses in the Y-branch, the propagation, and the output lens are approximately known and are all small (< 0.3 dB each), and the Fresnel loss at the waveguide/air interface is known, the input guide power can be calculated accurately from the measured output power. The interferometric modulator bias point was accurately determined by applying a 1-kHz sine wave to the electrodes and measuring the first- and second-harmonic outputs [11]. No dc bias was applied during these tests, so the optical damage measured was purely photovoltaic.

Devices with Ti-indiffused waveguides showed very good resistance to optical damage (with the exception detailed below). Figure 1-4 shows the bias point of two interferometric modulators as a function of illumination time. There was no bias point drift after 168 h with 100 mW in the input waveguide, and 21° drift after 200 h with 250 mW. The transmitted optical power dropped ≤ 0.3 dB during the 250-mW measurement. None of the other possible damage effects mentioned above were observed. One sample, though, which was tested at 430 mW for 30 h, had an optical transmission decrease of 0.6 dB and a drop in extinction from > 25 to 14 dB. The TE:TM ratio remained > 30 dB. The waveguides had elliptical modes with $1/e^2$-intensity dimensions of ~ 7.5 × 5.0 μm along Z and X, respectively, which gave a maximum intensity of about 0.75 MW/cm^2 in the 430-mW measurement. The size and shape of the mode did not seem to change significantly during the damage runs, but our measurement repeatability was limited to about ±1 μm and changes of that order or smaller could have occurred.

The PE waveguides showed susceptibility to optical damage, although by some measures they may be less sensitive than the Ti-indiffused waveguides. The phase bias drift of an interferometer was 18° after 200 h at 205 mW, which was comparable to the devices made with Ti-indiffused waveguides; this was accompanied by an optical transmission drop of ≤ 1 dB. In our measurements so far, the PE devices have shown no degradation of modulator extinction and have maintained their excellent polarization properties (TE:TM ratio > 41 dB). The maximum power at which these devices have been tested is 250 mW. We have not yet tested enough devices at high enough power levels to draw a conclusion about whether PE waveguides in $LiNbO_3$ offer better damage performance than Ti-indiffused waveguides in the 1320-nm wavelength range.

6
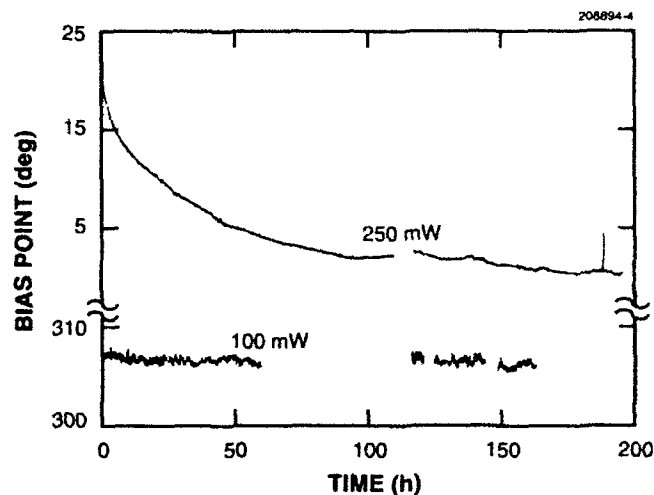
Figure 1-4. Bias point drift in interferometric modulators made using Ti-indiffused waveguides. Illumination was continuous; the gaps are recording failures.

One surprising result was that the damage susceptibility of Ti-indiffused waveguides was strongly dependent upon the final annealing process. An anneal in dry N_2 at temperatures as low as 120°C can significantly increase sensitivity to damage. This is of practical concern, since various post-diffusion processes may use dry N_2 anneals at elevated temperatures (our own problems occurred during a polyimide curing step), and also since devices in hermetically sealed packages are often backfilled with dry N_2 and may reach temperatures $\geq$120°C during their lifetime. With optical power levels on the order of 100 mW applied for a few hours, we have seen bias point drifts > 1000°, optical transmission drops as large as 3.6 dB, TE:TM ratio degradation to 22 dB, and extinction occasionally becoming as poor as 2 dB (the extinction often oscillates during damage). These damage effects are still mild compared to those at shorter wavelengths, but they are much worse than without the anneal. The increase in damage sensitivity can be reversed by an anneal in dry O_2; Table 1-1 summarizes the annealing effects on a test sample. A SiO_2 buffer layer can lessen the effects of a dry N_2 anneal. The test sample in Table 1-1 had no oxide layer over the Y-branches or input/output waveguides. A sample with a SiO_2 layer covering the entire device did not show an increase in damage susceptibility due to dry N_2 annealing at temperatures below 200°C. We have not yet tested PE guides for annealing effects.

In conclusion, we have found that the optical damage resistance of Ti-indiffused waveguides is good enough for most practical applications, but can be significantly degraded by a final anneal in dry N_2.

G. E. Betts
F. J. O'Donnell
K. G. Ray

7

TABLE 1-1

Effect of Annealing on a Ti-Indiffused LiNbO$_3$ Waveguide Sample

Anneal Prior to Test*	Operation		Bias Drift (deg)
	Power (mW)	Time (h)	
(As fabricated)	120	5	20
70 h, 40°C, dry N$_2$	123	5	13
16.5 h, 120°C, dry N$_2$	75	4	1240
3 h, 360°C, wet O$_2$	154	7	14
4 h, 500°C, dry O$_2$	131	22	3
1 h, 200°C, dry N$_2$	123	2.7	> 600
4 h, 500°C, dry O$_2$	126	6	15
*In chronological order.			

1.3 LINEAR ARRAYS OF STRAINED-LAYER InGaAs/AlGaAs DIODE LASERS

The fabrication and performance of individual InGaAs/AlGaAs quantum-well ridge waveguide diode lasers with applications as sources for free-space optical interconnections have been described previously [12]. Linear arrays of these low-threshold devices have now been developed, and the array performance and uniformity are reported here.

The linear arrays were fabricated in InGaAs/AlGaAs graded-index separate-confinement heterostructure (SCH) double-quantum-well (DQW) laser structures grown on n^+-GaAs substrates by organometallic vapor phase epitaxy [13]. The detailed cross section of the ridge waveguide structure is given in [12]. Two InGaAs quantum wells in the active region are sandwiched between upper p-type and lower n-type AlGaAs cladding layers, as illustrated in the inset of Figure 1-5. The ion-beam-assisted etching of the ridges and the thin-film deposition procedures used in the laser fabrication have also been described previously [12]. The total ridge depth (etch depth) for these lasers is on the order of 1 μm. Laser arrays containing thirty 2-μm-wide ridge lasers and several 3-μm-wide ridge lasers on one end were cleaved into bars that had cavity lengths in the range 160–500 μm. The center-to-center laser spacing is 150 μm. Several pieces of the same wafer were etched to different depths to determine the effect of cladding thickness outside the ridge. The laser array performance was characterized using light output vs pulsed current measurements (300-ns pulses at 1 kHz).

Figure 1-5. Plots of (a) average pulsed threshold current and (b) average differential quantum efficiency, both as a function of the upper cladding thickness t (see inset) for 2-µm-wide, 500-µm-long uncoated ridge waveguide laser arrays.

Figure 1-5 shows the average threshold current I_{th} and differential quantum efficiency η_d vs the average upper cladding thickness outside the ridge, t, for 500-μm-long uncoated laser bars. Each bar was cleaved from a separately fabricated sample of the same wafer. The parameter t was varied from 40 to 310 nm ($\pm$20 nm over a 1-cm^2 sample) by controlling the depth of the ion-beam-assisted etch. The error bars indicate the extrema of the measured data across a single laser bar. The data of Figure 1-5(a) show that minimum threshold currents of 6–7 mA are achie' .d for t values between 160 and 240 nm. The I_{th} increases to 8–10 mA for $t \geq 310$ nm and 15–18 mA ' $t \leq 40$ nm. The η_d was measured to be $\geq 40\%$ for all thicknesses ≥ 160 nm. These data indicate that low-threshold and high-efficiency lasers can be made for $t = 200 \pm 40$ nm. This represents a tolerance in the etch depth of approximately $\pm4\%$.

The effect of device length on threshold and efficiency for the three best wafers with $t = 160, 170,$ and 240 nm are plotted in Figure 1-6, where each point represents an average value of I_{th} or η_d for the 2-μm-wide lasers. The shorter devices generally tend to have the lowest threshold currents and highest efficiencies. Devices with cavity lengths between 160 and 300 μm routinely exhibited thresholds < 5 mA and efficiencies > 42% per facet. The best lasers on the 160- and 200-μm-long bars exhibited threshold currents and efficiencies of 3.8 mA and $\geq 46\%$ per facet, respectively.

A histogram showing the distribution of I_{th} and η_d of a 200-μm-long, uncoated bar having thirty 2-μm-wide lasers is shown in Figure 1-7. Greater than 90% of all the elements and 17 consecutive lasers exhibited threshold currents of 4.2 $\pm$ 0.4 mA with efficiencies of 46 $\pm$ 2% per facet. Only two out of the 30 lasers had threshold currents > 5 mA. A ten-element array of 3-μm-wide ridge lasers from the same 200-μm-long bar had only a slightly higher I_{th} (4.7 $\pm$ 0.5 mA) and essentially the same η_d. A 30-element array of 2-μm-wide lasers with a 500-μm-long cavity was also extremely uniform and had I_{th} and η_d of 6.0 $\pm$ 0.5 mA and 42 $\pm$ 1.5% per facet, respectively. The small spread of these distributions demonstrates the feasibility of fabricating linear arrays of ridge waveguide diode lasers that exhibit uniform performance characteristics and that will be important for low-skew optical interconnections.

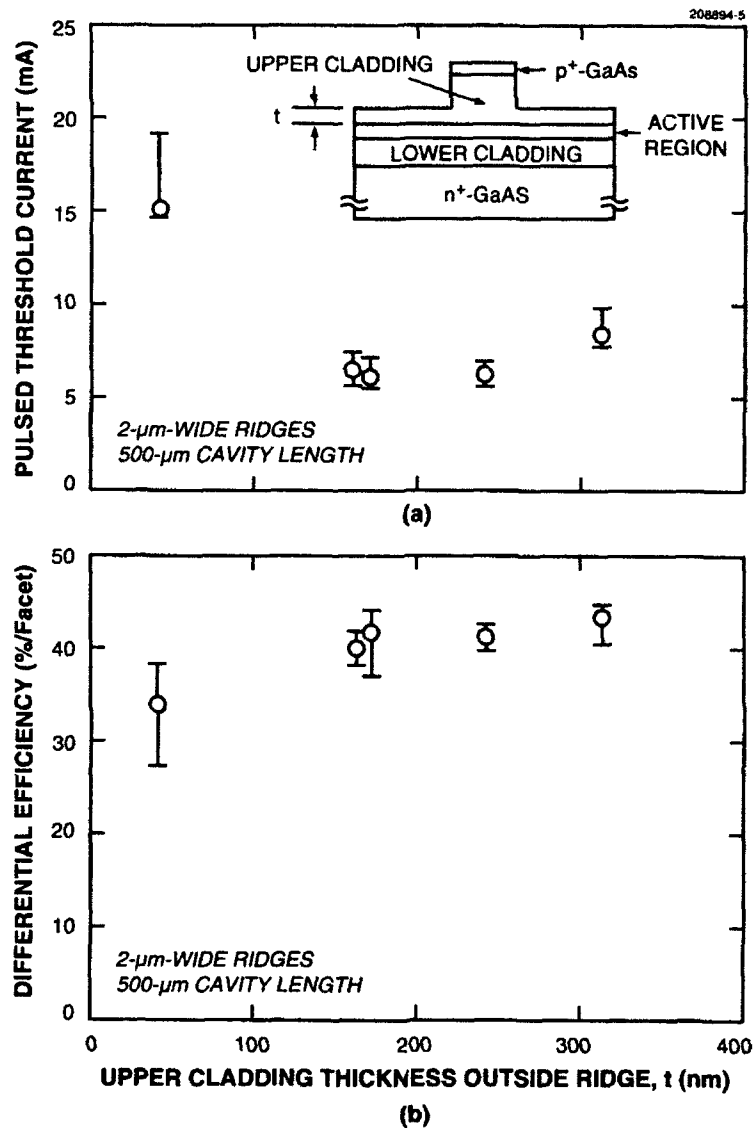J. D. Woodhouse   R. J. Bailey
J. P. Donnelly   D. Z. Tsang
C. A. Wang
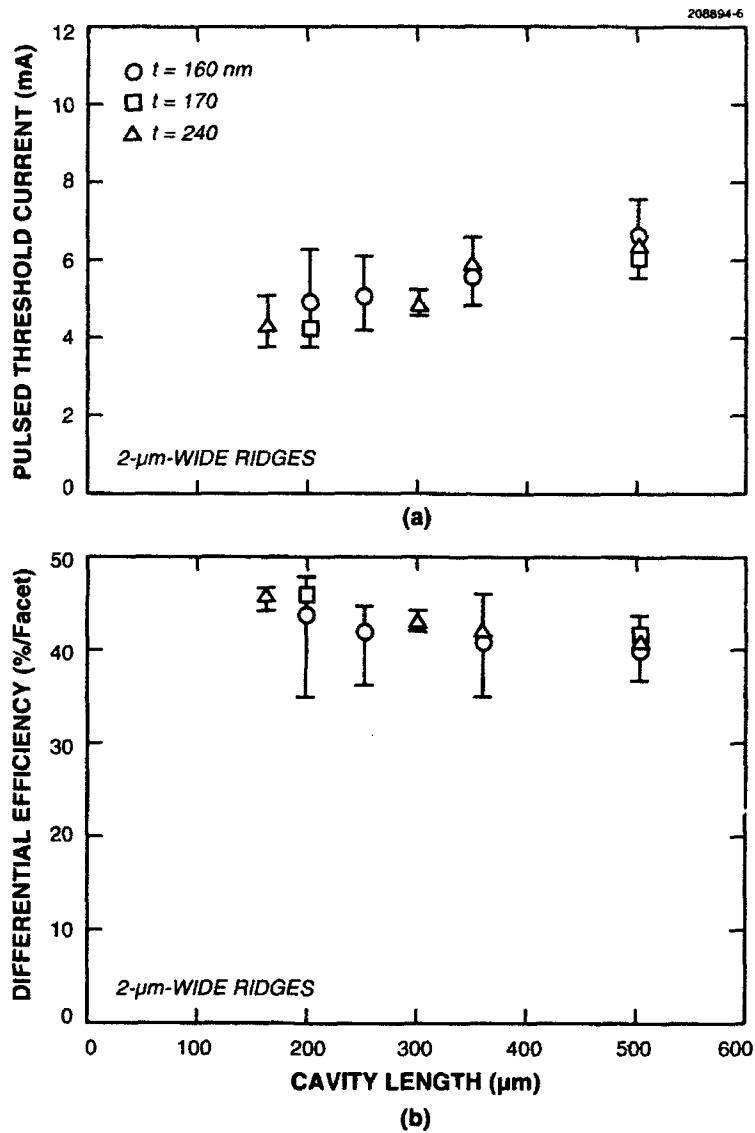
Figure 1-6. Plots of (a) average pulsed threshold current and (b) average differential quantum efficiency, both as a function of cavity length, for 2-µm-wide uncoated ridge waveguide laser arrays having t values of 160, 170, and 240 nm.
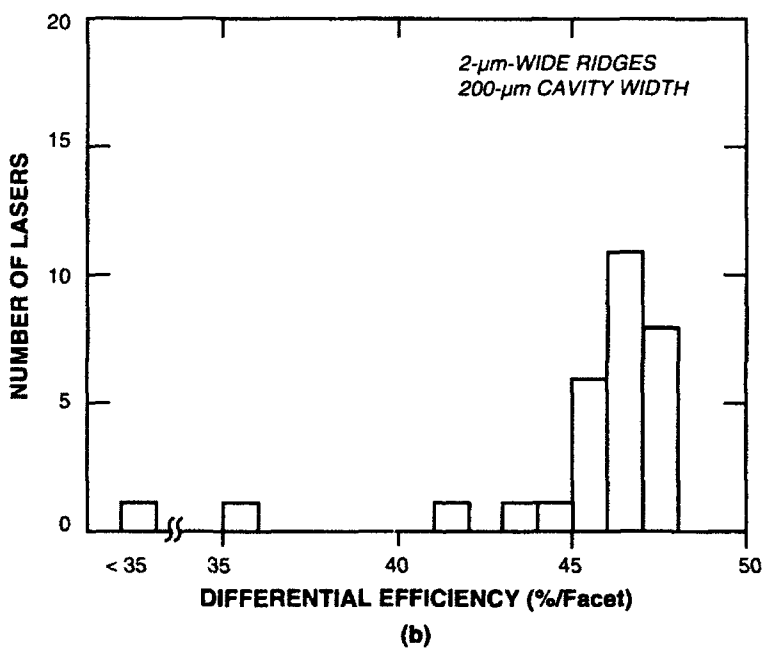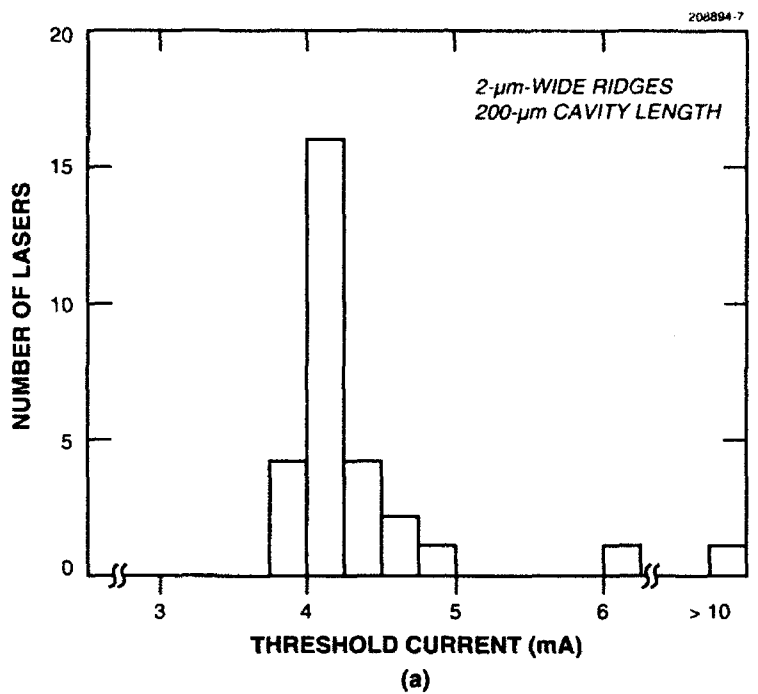
Figure 1-7. Histograms showing the distribution of the number of lasers as a function of (a) pulsed threshold current and (b) differential quantum efficiency for a 30-element linear array of 2-μm-wide, 200-μm-long uncoated ridge waveguide lasers.

REFERENCES

1. A. R. Clawson, W. Y. Lum, and G. E. McWilliams, *J. Cryst. Growth* **46**, 300 (1979).

2. G. A. Antypas, *Appl. Phys. Lett.* **37**, 64 (1980).

3. R. F. Karlicek, Jr., D. Mitcham, J. C. Ginocchio, and B. Hammarlund, *J. Electrochem. Soc.* **134**, 470 (1987).

4. G. B. Stringfellow, *Organometallic Vapor Phase Epitaxy: Theory and Practice* (Academic, San Diego, 1989), pp. 171-173.

5. Z. L. Liau, *Appl. Phys. Lett.* **58**, 1869 (1991).

6. *American Institute of Physics Handbook*, D. E. Gray, ed. (McGraw-Hill, New York, 1972), pp. 4–299.

7. G. T. Harvey, G. Astfalk, A. Y. Feldblum, and B. Kassahun, *IEEE J. Quantum Electron.* **QE-22**, 939 (1986).

8. G. E. Betts, L. M. Johnson, and C. H. Cox III, *Proc. SPIE* **1562**, 281 (1991).

9. A. M. Glass, *Opt. Eng.* **17**, 470 (1978).

10. J. F. Lam and H. W. Yen, *Appl. Phys. Lett.* **45**, 1172 (1984).

11. G. E. Betts and L. M. Johnson, *Proc. SPIE* **835**, 152 (1987).

12. Solid State Research Report, Lincoln Laboratory, MIT, 1992:2, p. 5.

13. C. A. Wang, *Lincoln Lab. J.* **3**, 3 (1991).

2. QUANTUM ELECTRONICS

2.1 DIODE-PUMPED, Q-SWITCHED Yb:YAG LASER

As a gain medium for diode-pumped lasers, Yb:YAG offers several advantages relative to Nd:YAG. These include larger absorption bandwidth for reduced sensitivity to diode wavelength changes, longer upper-state lifetime for higher-energy storage, and lower thermal loading for reduced thermooptic distortion. The Yb:YAG lasers are pumped at 0.94 μm, oscillate at 1.03 μm, and exhibit efficient CW room-temperature laser operation despite being quasi-three-level at this temperature [1],[2]. In addition, models indicate that efficient operation in an energy storage mode should be possible. Here, we describe the first diode-pumped, Q-switched Yb:YAG laser.

A schematic of the experiment is shown in Figure 2-1. Two InGaAs diode lasers with a stripe width of 75 μm and up to ~ 500-mW output power are collimated using gradient-index lenses in combination with a cylindrical lens of 6-cm focal length. The beams are focused into the Yb:YAG by geometric multiplexing [3] with a lens of 2.5-cm focal length. The pump spot radius was ~ 40 μm at the focus. The Yb:YAG gain element is doped with 15-at.% Yb^{3+}. The Yb:YAG gain element is 0.11 cm thick and is polished flat and parallel; this thickness is equal to ~ 1.5 unsaturated absorption lengths at the pump wavelength of 0.94 μm. It is coated on one face with a mirror with high reflectivity at 1.03 μm and high transmission (83%) at 0.94 μm and on the other face with a single-layer antireflection (AR) coating at 1.03 μm. An AR-coated, 1.1-cm-long $LiNbO_3$ crystal in combination with a thin-film polarizer and a quarter-wave plate is used for the electrooptic Q switch. The output coupler is a 20% transmission mirror with 10-cm radius of curvature and is placed so that the cavity is nearly hemispherical.
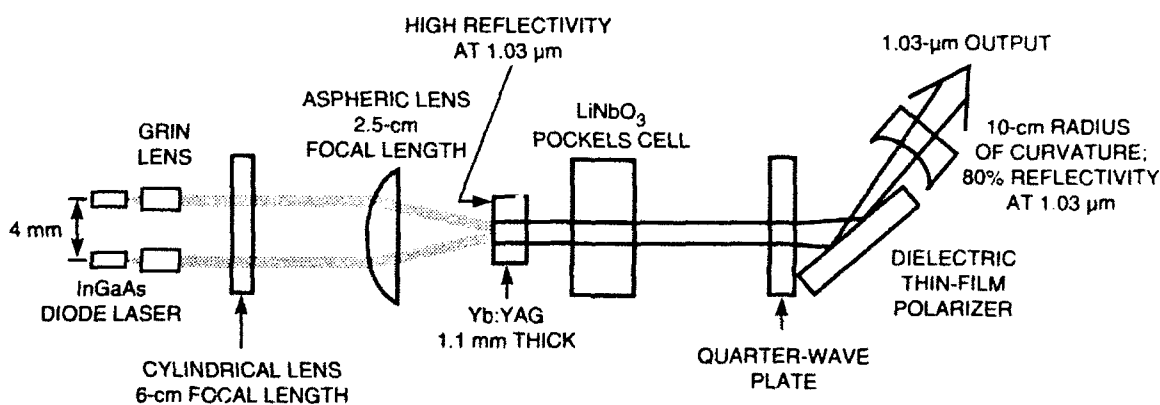
Figure 2-1. Schematic of the Q-switched Yb:YAG laser. The diode junction is perpendicular to the plane of the page. The cylindrical lens acts on the plane of the junction.

15
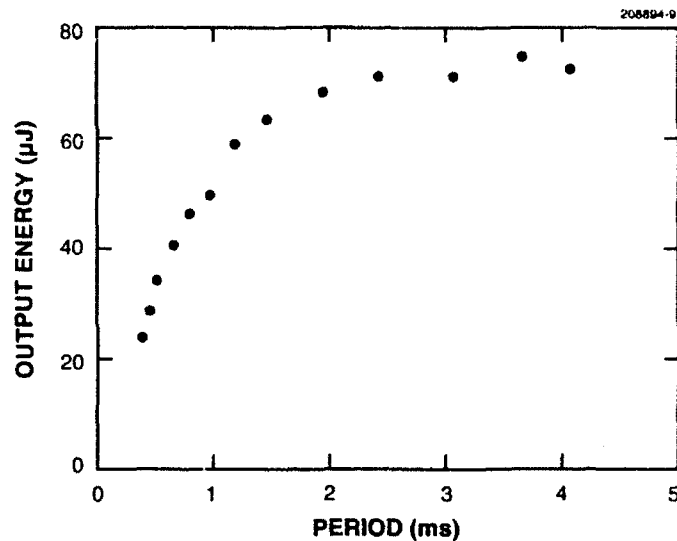
Figure 2-2. Output energy per pulse at 1.03 μm as a function of the period between pulses for 720-mW incident power on the gain element at 0.94 μm.

The Q-switched energy per pulse as a function of the period between pulses is shown in Figure 2-2 for an incident pump power of 720 mW on the Yb:YAG. Up to 72-μJ output energy per pulse was attained in the low-repetition-rate limit; at this output energy the output pulse width was 11 ns (full width at half-maximum). In the high-repetition-rate limit the average power of the laser was 71 mW, corresponding to a 10% optical to-optical efficiency. The TEM_{00} mode radius in the Yb:YAG gain element was ~ 40 μm based on measurements of the output beam divergence.

Higher-efficiency operation should be possible in this laser with more optimized design: models indicate that ~ 30% optical-to-optical efficiency may be obtained for the pump intensity used in this experiment [4]. In the laser described here, the pump radiation is passed through the gain element only once; however, double passing of the pump radiation in quasi-three-level lasers can provide a large increase (~ 50%) in efficiency relative to single-pass pumping. In addition, the efficiency can be increased by choosing the optimum gain element length. The gain element must be long enough to efficiently absorb the pump radiation, but cannot be so long that not all of the gain element is pumped sufficiently hard to achieve population inversion. Calculations indicate that the gain element needs to be 2.1 unsaturated absorption lengths (at the pump wavelength) for optimum efficiency at high repetition rates (> 2 kHz) and even longer at low repetition rates. Clearly, the gain element length used in this experiment (1.5 unsaturated absorption lengths) is too short.

One of the key issues in Q-switched Yb:YAG lasers is damage, because the saturation fluence at 1.03 μm is ~ 10 J/cm^2 and, for efficient short-pulse extraction, the extracting fluence must be on the order of the saturation fluence. This saturation fluence is beginning to approach the damage fluence of optics

16

and coatings for pulses of a few nanoseconds. The intracavity circulating fluence at the lowest repetition rates in our Q-switched Yb:YAG laser is ~ 7 J/cm^2. However, despite the short pulse length of 11 ns, no damage was observed during this experiment.

T. Y. Fan

REFERENCES

1. T. Y. Fan, *Lincoln Lab. J.* **3**, 413 (1990).

2. P. Lacovara, H. K. Choi, C. A. Wang, R. L. Aggarwal, and T. Y. Fan, *Opt. Lett.* **16**, 1089 (1991).

3. T. Y. Fan, W. E. DeFeo, and A. Sanchez, *Opt. Lett.* **14**, 1057 (1989).

4. T. Y. Fan, to be published in *IEEE J. Quantum Electron.* **28** (1992).

3. MATERIALS RESEARCH

3.1 CRITICAL LAYER THICKNESS OF STRAINED-LAYER InGaAs/GaAs MULTIPLE QUANTUM WELLS DETERMINED BY DOUBLE-CRYSTAL X-RAY DIFFRACTION

Diode lasers with an active region consisting of several strained-layer InGaAs quantum wells separated by GaAs barriers are of interest for high-speed optical data transmission. In designing such multiple-quantum-well (MQW) InGaAs/GaAs devices, it is important to keep the total effective strain energy low enough to avoid lattice relaxation by the formation of misfit dislocations that reduce the efficiency and operating lifetime of the device. Numerous experimental observations of the onset of relaxation for InGaAs/GaAs single quantum wells (SQWs), which determines the critical layer thickness h_c, have been correlated with the Matthews and Blakeslee (MB) force-balance model [1] with misfit dislocations generated by the double-kink mechanism. However, strain relaxation dependent on the barrier layer thickness has been observed in strained-layer superlattices, even though the thickness of each strained quantum well is below h_c [2]. We report h_c for strained InGaAs/GaAs MQWs by using Nomarski contrast microscopy and double-crystal x-ray diffraction to detect the onset of strain relaxation. For MQWs, h_c depends on the thickness of the GaAs barrier layer and can be described by the MB model, assuming misfit dislocations formed by the single-kink mechanism.

The MQW structures were grown by organometallic vapor phase epitaxy in a vertical rotating-disk reactor on n^+-GaAs substrates oriented 2° off (001) toward the nearest [110]. The source materials were trimethylgallium, trimethylindium (TMI), and 100% arsine. The vapor pressure of the TMI was monitored with an ultrasonic transducer to ensure that the source was stable and that the InAs mole fraction in the strained quantum wells was controlled to within ±0.2%. The InGaAs/GaAs MQW layers were grown at 625°C and a V/III ratio of 300 on a 0.4-μm-thick GaAs buffer layer. The thickness of the $In_{0.16}Ga0_{.84}As$ quantum well was 10 nm, the thickness of the GaAs barrier layer t_B ranged from 8 to 55 nm, and the number of periods q ranged from 1 to 15. The samples were characterized by means of Nomarski contrast microscopy, low-temperature photoluminescence (PL), and double-crystal x-ray diffraction.

In the first set of experiments, t_B was kept constant at 55 nm and q was varied from 1 to 15. Table 3-1 summarizes surface morphology observations and the PL data. The surface morphology was smooth and featureless for $q = 6$ or less but very slightly crosshatched for $q = 7$, indicating that the structure had undergone some relaxation to accommodate the increasing strain energy. With increasing q, the morphology became increasingly crosshatched. However, the PL spectra measured at 6 K gave little indication of lattice relaxation. The peak position, intensity, and width remained nearly constant for all structures. Even for the sample with $q = 15$, the full width at half-maximum (FWHM) was only 4 meV, compared with 2 meV for the SQW sample. The PL results are in contrast to the report of [2] that shows a decrease in PL peak intensity, increase in FWHM, and decrease in PL energy associated with strain relaxation.

TABLE 3-1

Properties of Strained-Layer InGaAs/GaAs MQW Structures

q	Surface Morphology	Photoluminescence Data	
		Peak Energy (eV)	FWHM (meV)
1	Smooth	1.3525	2
3	Smooth	1.3500	3
5	Smooth	1.3510	3.5
6	Smooth	1.3485	4
7	Crosshatched	1.3520	3.5
10	Crosshatched	1.3515	3.5
15	Crosshatched	1.3515	4

Figure 3-1 shows simulated and experimental double-crystal x-ray diffraction rocking curves for the same MQW structure with various values of q. The simulated curves were obtained using software based on the Taupin-Tagachi solution to dynamical x-ray diffraction theory. The InGaAs layers were assumed to be completely strained. In general, the curves consist of a set of satellite peaks resulting from the MQW periodicity. The MQW structure period determines the spacing of these satellite peaks. The average InGaAs composition of the structure $x_{av} = x[t_w/(t_w + t_B)]$, where t_w is the thickness of the quantum well, determines the location of the $n = 0$ satellite, and the InGaAs composition determines the position of the broad satellite envelope. The simulation curves in Figure 3-1(a) show that as q increases, the FWHM of the satellite peaks decreases. In addition, between each adjacent satellite peak there are exactly $q-2$ interference fringes. The experimental rocking curves in Figure 3-1(b) show a decrease in FWHM of the satellite peaks with increasing periods up to 6–7, and then an increase. In Figure 3-2 the experimental and simulated rocking curves are shown in greater detail for $q = 6$ and 7 between $n = 6$ and 7 satellite peaks. The interference fringes are well resolved for $q = 6$. However, for $q = 7$, the nearest interference fringe on the low-angle side of the satellite peaks becomes less distinct. For $q = 10$, the interference fringes are no longer resolved and the satellite peaks are significantly broadened, and for $q = 15$, the satellite peak intensity decreases. The onset of broadening in the rocking curves is consistent with the observation of a crosshatched morphology, suggesting that double-crystal x-ray diffraction can be used to detect the onset of relaxation in strained-layer MQWs.
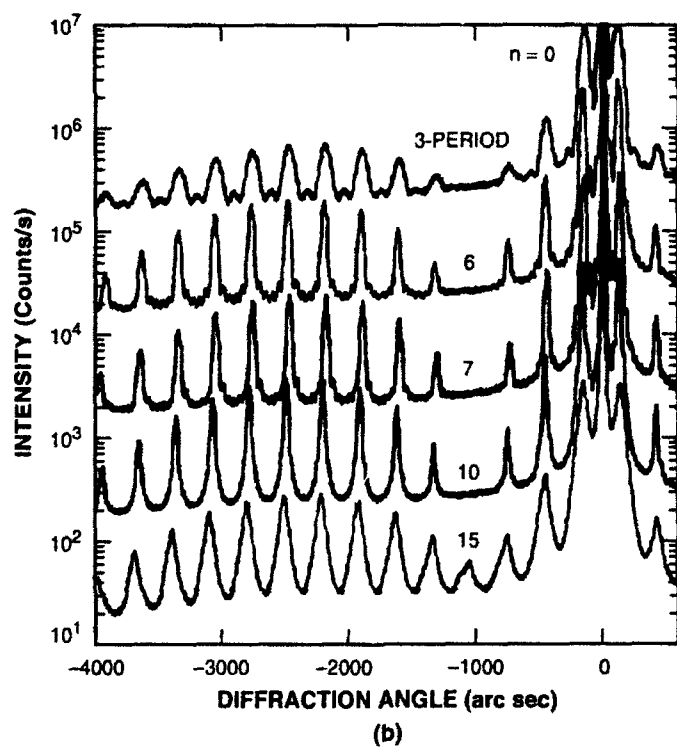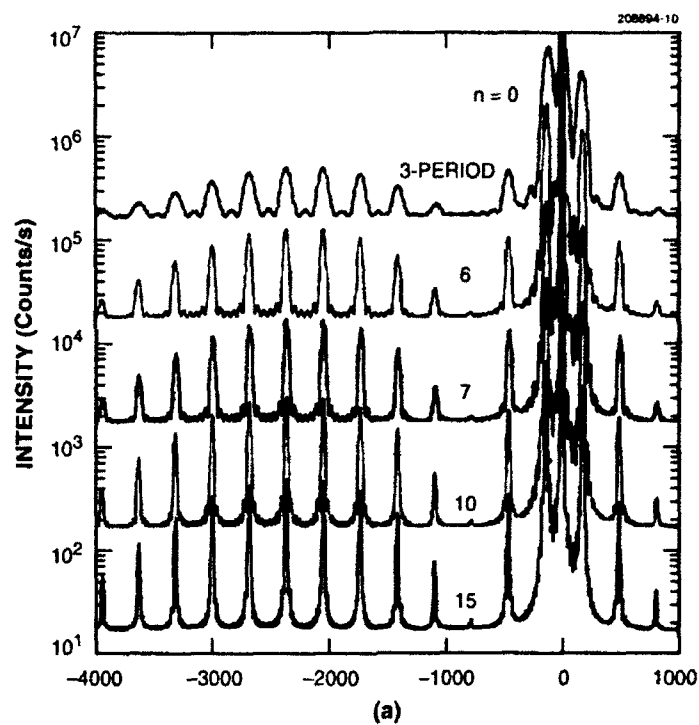
Figure 3-1. Double-crystal x-ray diffraction rocking curves of InGaAs/GaAs MQW structure: (a) simulation and (b) experiment.

21
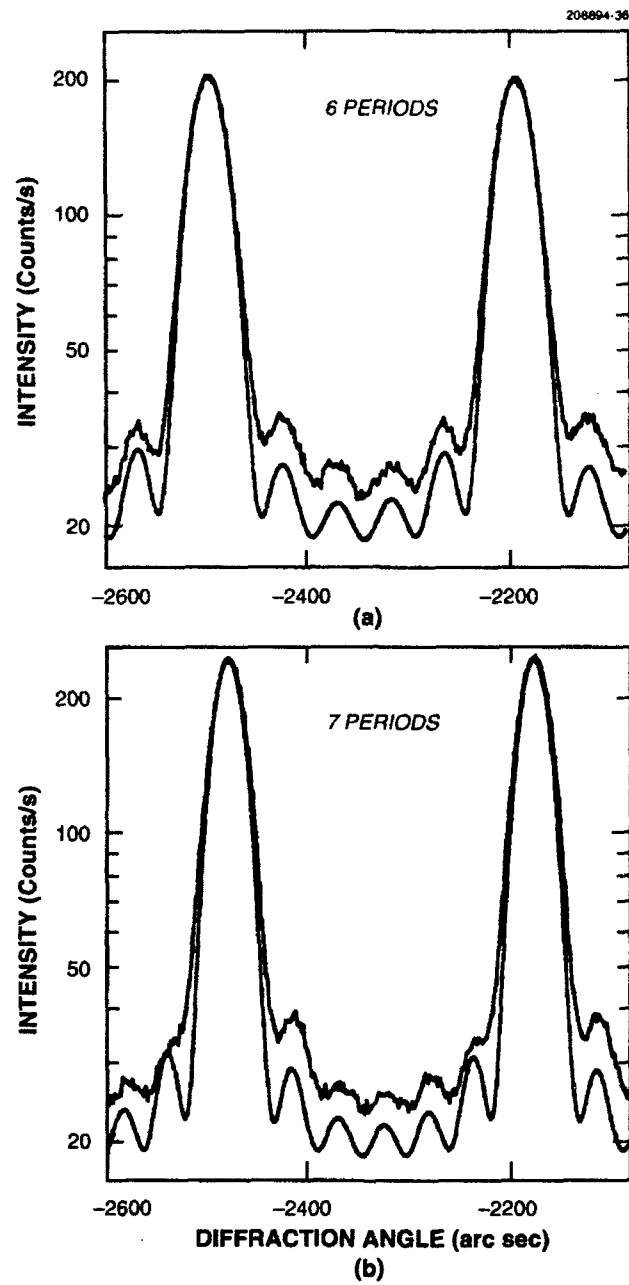
Figure 3-2. Rocking curves of Figure 3-1 between n = 6 and 7 satellite peaks for (a) 6 periods and (b) 7 periods, obtained by simulation (lower) and experiment (upper).
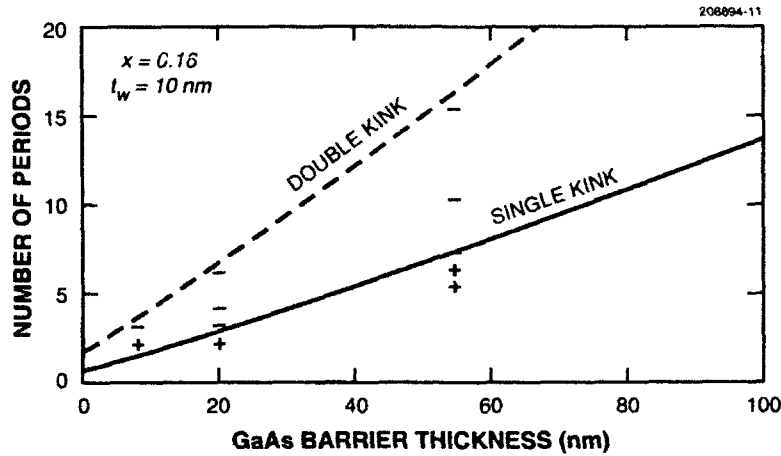
Figure 3-3. Number of periods q as a function of GaAs barrier thickness t_B with x = 0.16 and t_w = 10 nm. A plus (+) indicates a smooth surface morphology, while a minus (−) indicates a crosshatched morphology.
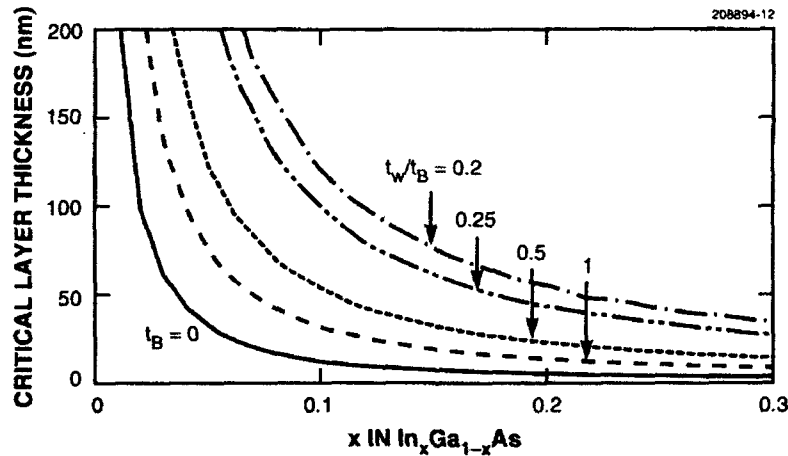
Figure 3-4. Critical layer thickness h_c for InGaAs/GaAs MQWs as a function of InAs mole fraction x for different ratios of t_w to t_B calculated from the Matthews and Blakeslee model for the single-kink mechanism.

To determine the number of periods in an MQW structure that can be grown without strain relaxation, h_c as given by the MB force-balance model is divided by t_w. Since it is unknown a priori if misfit dislocation generation is by the single- or double-kink mechanism, h_c is calculated for x_{av} for both cases. Figure 3-3 shows the calculated boundary between strained and relaxed structures for an MQW sample with x = 0.16 and t_w = 10 nm on a plot of q vs t_B. Below each curve the layers are expected to

23

be completely strained, and above the curves lattice relaxation is expected. Experiments were then carried out in which MQW samples with various t_B and q were grown. The surface morphology observed for these samples is indicated in Figure 3-3. A plus (+) indicates a smooth surface morphology, while a minus (−) indicates a crosshatched morphology. Our data for 20- and 55-nm GaAs barriers are consistent with the q values calculated according to the single-kink dislocation mechanism. A more general plot of h_c vs x for different ratios of t_w to t_B is shown in Figure 3-4. As expected, h_c increases as t_w/t_B decreases. Note that the $t_D = 0$ case corresponds to a single, uncovered layer of InGaAs.

C. A. Wang   S. H. Groves
J. H. Reinold   D. R. Calawa

3.2 NORMAL-INCIDENCE INTERSUBBAND ABSORPTION IN n-TYPE ELLIPSOIDAL-VALLEY QUANTUM WELLS

Since the first observation [3] of intersubband transitions in GaAs quantum wells, considerable interest has developed in using such transitions as the basis for 8–12-μm infrared photodetectors. Because the conduction-band electrons in n-type GaAs quantum wells occupy spherical constant-energy surfaces, the intersubband transitions occur only for the component of the incident photon polarization that is perpendicular to the plane of the quantum well. Since normally incident radiation is not absorbed, practical n-type GaAs quantum-well photodetectors must utilize complex structures such as 45° facets or sawtooth gratings. However, according to our recent calculation [4], strong intersubband absorption should be exhibited at normal incidence by electrons occupying ellipsoidal constant-energy surfaces in indirect-bandgap quantum wells. Here, we report [5] the observation of such normal-incidence absorption in n-type $Al_{0.09}Ga_{0.91}Sb$ quantum wells. We also report the observation of intersubband absorption in direct-bandgap GaSb quantum wells.

The quantum-well samples were grown by molecular beam epitaxy (MBE) on (100) n-type GaSb substrates. The sources for MBE growth were Al, Ga, As, and Sb, with GaTe used for n-type doping. For the n-type $Al_xGa_{1-x}Sb$ samples, x was large enough and the wells narrow enough that electrons occupied the four equivalent ellipsoids lying along the <111> axes at the L points. For comparison, we also investigated n-type GaSb quantum wells in which electrons occupy a single spherical valley at the Γ point. Two ellipsoidal-valley samples contained 100 $Al_{0.09}Ga_{0.91}Sb$ wells, 6.4 and 7.0 nm thick, respectively, while a spherical-valley sample contained 50 GaSb wells, 11.0 nm thick. In all samples, electrons were confined by 20-nm-thick $AlAs_{0.08}Sb_{0.92}$ barrier layers lattice matched to GaSb. In the AlGaSb sample with 7.0-nm-thick wells and the GaSb sample, the wells and barriers were doped with Te donors to 2.5×10^{17} cm^{-3}. In the AlGaSb sample with 6.4-nm-thick wells, the wells were doped to 1×10^{18} cm^{-3} and the barriers were undoped. The measured x-ray diffraction rocking curves are in good agreement with curves simulated for the intended structures. The peak energy of the 4.5-K PL measured from the sample with 7.0-nm-thick wells is 1.04 eV, compared with a calculated value of 1.02 eV.

Infrared transmission spectra were measured at Brewster's angle and at normal incidence with a Fourier transform spectrometer. In Figure 3-5, showing the room-temperature spectra from the AlGaSb sample with 7.0-nm-thick wells, each spectrum was normalized to the corresponding spectrum from a bare GaSb substrate, and multiple-pass interference fringes arising from reflections within the epitaxial

layers were cancelled numerically. Strong room-temperature absorption is observed both at Brewster's angle and at normal incidence. The absorption peaks that are located at 870 cm^{-1} (11.5 μm) at Brewster's angle and 800 cm^{-1} (12.5 μm) at normal incidence are due to transitions between the first and second L subbands. The peak absorption strength is ~ 10% at both Brewster's angle and normal incidence, in good agreement with the theoretical strength. The normal-incidence absorption peak appears at lower energy because of imperfect cancellation of the large interference fringes that occur at normal incidence. The absorption peak of the AlGaSb sample with 6.4-nm-thick wells (not shown) is shifted by 180 cm^{-1} to higher energy, in close agreement with the expected shift for an intersubband transition.

In addition, we have studied the persistent photoabsorption at 77 K in the same AlGaSb sample as in Figure 3-5. Shown in Figure 3-6 are the transmission spectra obtained by normalizing the spectra measured after white-light illumination to the corresponding spectra measured before illumination. Illumination enhances the intersubband absorption, both at Brewster's angle and at normal incidence, presumably because photoionization of electron traps increases the electron density in the quantum wells. Figure 3-7 compares the 77-K transmission spectra of the AlGaSb sample with 7.0-nm-thick wells and the GaSb sample taken at Brewster's angle without white-light illumination. The absorption peak at 1060 cm^{-1} (9.4 μm) for the GaSb sample is due to transitions between the first and second Γ subbands. Because the electrons in the GaSb sample occupy spherical-valley quantum wells, intersubband absorption is not observed at normal incidence.
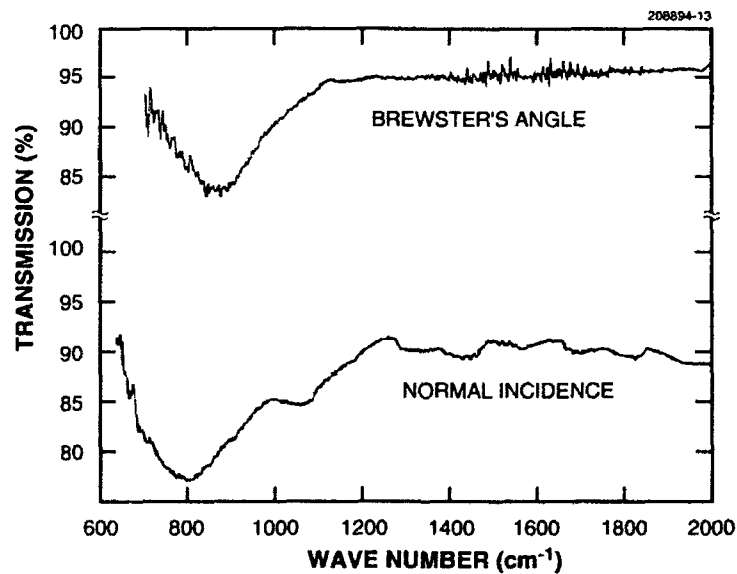
Figure 3-5. Brewster's-angle and normal-incidence transmission spectra of an indirect-bandgap $Al_{0.09}Ga_{0.91}Sb$ quantum-well sample measured at room temperature.
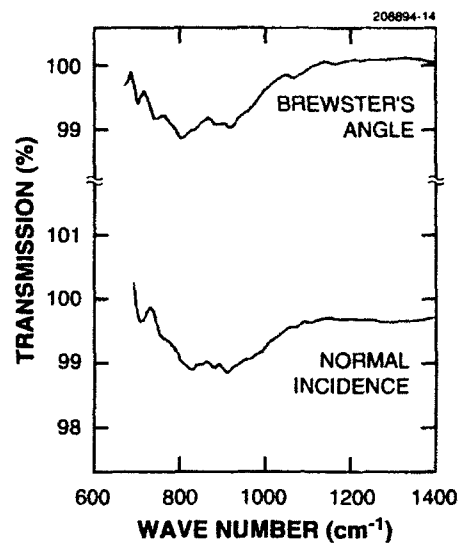
Figure 3-6. Normalized transmission spectra showing persistent photoabsorption at 77 K in the $Al_{0.09}Ga_{0.91}Sb$ quantum-well sample of Figure 3-4.
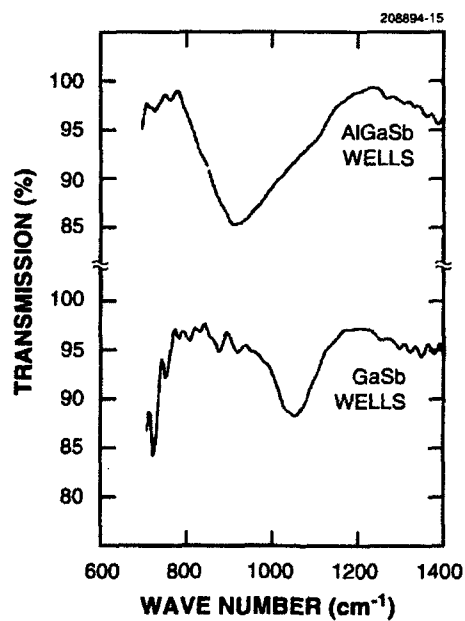
Figure 3-7. Brewster's-angle transmission spectra of indirect-bandgap AlGaSb and direct-bandgap GaSb quantum-well samples measured at 77 K.

The ability of ellipsoidal-valley quantum wells to absorb normally incident radiation should overcome the radiation-coupling difficulties of conventional spherical-valley quantum wells and permit the development of improved detectors for focal plane arrays. In addition, ellipsoidal-valley photodetectors are expected to exhibit higher detectivity than spherical-valley detectors because the ellipsoidal-valley devices are predicted to have a higher fractional absorption per quantum well and a lower dark current.

S. J. Eglash   K. A. McIntosh

E. R. Brown   J. V. Pantano

REFERENCES

1. J. W. Matthews and A. E. Blakeslee, *J. Cryst. Growth* **27**, 118 (1974).

2. R. Grey, J. P. R. David, P. A. Claxton, F. Gonzalez Sanz, and J. Woodhead, *J. Appl. Phys.* **66**, 975 (1989).

3. L. C. West and S. J. Eglash, *Appl. Phys. Lett.* **46**, 1156 (1985).

4. E. R. Brown and S. J. Eglash, *Phys. Rev. B* **41**, 7559 (1990).

5. E. R. Brown, S. J. Eglash, and K. A. McIntosh, *Phys. Rev. B* **46**, 7244 (1992).

4. SUBMICROMETER TECHNOLOGY

4.1 WET-DEVELOPED BILAYER RESISTS FOR 193-nm EXCIMER LASER LITHOGRAPHY

Silicon-polymer bilayer resists have been demonstrated for several years [1]. In particular, the polysilynes, because of their unusual combination of photosensitivity, solubility, and atomic composition, have been found promising as both wet- [2] and dry-developed [3] resists for use at 193 nm. The polysilynes contain over 30-wt% silicon and, as will be shown below, can be synthesized so that they have both good film-forming properties and high photosensitivity. Essentially, the composition and molecular weight can be adjusted so that only mild crosslinking is required to render the film insoluble, resulting in a sensitive, single-component, negative-tone resist.

The silyne homopolymers can be divided into two categories, those with linear pendant groups and those with branched pendant groups. The linear-group-substituted polymers are generally high in molecular weight and exhibit poor solubility, whereas the branched-group-substituted systems have low molecular weight and poor photosensitivity. The molecular weights of the latter group are limited by steric hindrance during polymerization. The molecular weight of a linear-group-substituted polymer can also be kept low, however, either by copolymerization or by adding chain-terminating reagents during synthesis. These reductions in molecular weight render the polymer completely soluble and result in a system that can be readily spin cast into thin, uniform films. Fortunately, the changes in molecular weight are accompanied by relatively small decreases in photosensitivity, as seen in Figure 4-1.
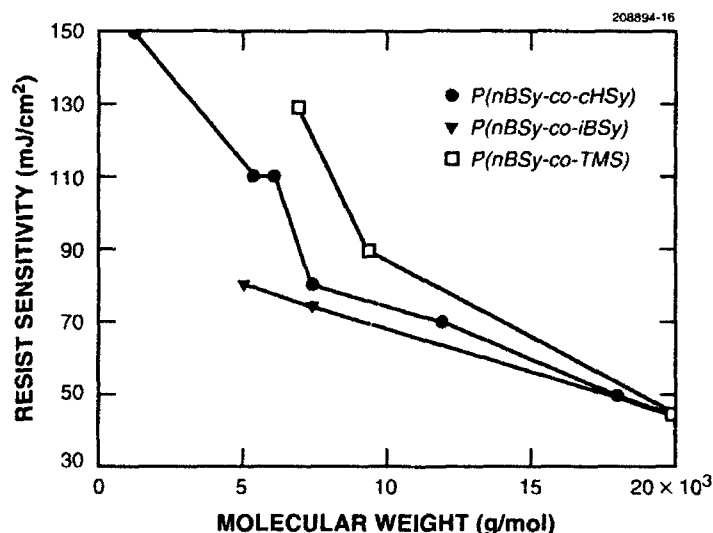

Figure 4-1. Resist sensitivity vs molecular weight for three resist formulations based on a majority of n-butyl silyne monomer.

Optimal formulations for several base polymers were obtained using copolymerization and chain-terminating reagents, and the results are summarized in Table 4-1. In general, these systems require 35–85-mJ/cm^2 sensitivity at 193 nm to become insoluble. It is important to note, however, that the sensitivity is dependent not only upon molecular weight but also upon the polymer's solubility parameter, as dictated by its pendant R-group. For example, a cyclohexyl group has a solubility parameter roughly three times that of a methyl group [4]. This value means that, all other things being equal, a polysilyne having pendant methyl in place of pendant cyclohexyl will require fewer crosslinks to prohibit solvation and dissolution by the developer. This argument is an important consideration when designing a copolymer system.

TABLE 4-1

Optimized Formulations for Several Base Silyne Polymers

Base Polymer	Additive	Loading (%)	Molecular Weight (g/mol)	Sensitivity (mJ/cm^2)
Copolymers				
Poly(n-butyl silyne)	Poly(cyclohexyl silyne)	20	7 000	80
Poly(n-butyl silyne)	Poly(isobutyl silyne)	30	6 258	72
Poly(n-propyl silyne)	Poly(cyclohexyl silyne)	20	8 676	50
Poly(n-propyl silyne)	Poly(isobutyl silyne)	40	Not measured	34
Poly(methyl silyne)	Poly(isobutyl silyne)	40	12 441	36
Chain-terminated polymers				
Poly(n-propyl silyne)	Trimethylsilyl	23	5 827	75
Poly(n-butyl silyne)	Trimethylsilyl	10	9 047	90

Additional improvements to the sensitivities shown in Table 4-1 can be obtained by either of two methods. First, electrophilic sensitizing agents, such as 2,4,6-trichloromethyl-1,3,5-triazine, can be added. These agents act similarly to those proposed for positive-tone silicon-polymer resists [5], where pendant aryl groups must be present to allow efficient electron transfer between the polymer backbone and the sensitizer. The enhancement in sensitivity depends on the number of pendant aryl groups, with a 2 times improvement observed for 100% aliphatic-substituted systems and a 6 times improvement for 100% aromatic-substituted systems. An alternative method for improving the photosensitivity of polysilynes involves preparation of the polysilyne with an electron-withdrawing group pendant directly to the backbone. This method requires the polymer to initially contain pendant phenyl groups, which act as

substitution sites for the sensitizers [6]. Although control of the substitution reaction has not yet been optimized, sensitivities in the range 1–10 mJ/cm^2 have been obtained for several different substituents.

The evaluation of the lithographic properties of the polysilyne films was performed with projection imaging on a 0.22-numerical-aperture (NA) catadioptric 5× reduction lens, operating at 193 nm [7]. The laser operated with an unnarrowed bandwidth at a pulse repetition rate of 400 Hz, delivering roughly 0.3 mJ/cm^2 per pulse at the wafer plane. Following development in toluene, the patterned wafers were etched in an oxygen plasma, using either a parallel-plate RF discharge, or a helical-wave RF etcher (helicon). The linewidth metrology was performed on a modified electron microscope equipped with a commercially available automated wafer inspection system.

Once a number of optimized formulations were prepared, it became apparent that not all the resists have similar lithographic performance. Figure 4-2(a) shows a poly(methyl silyne) base polymer reduced

1 µm   (a)
1 µm   (b)
1 µm   (c)
1 µm   (d)
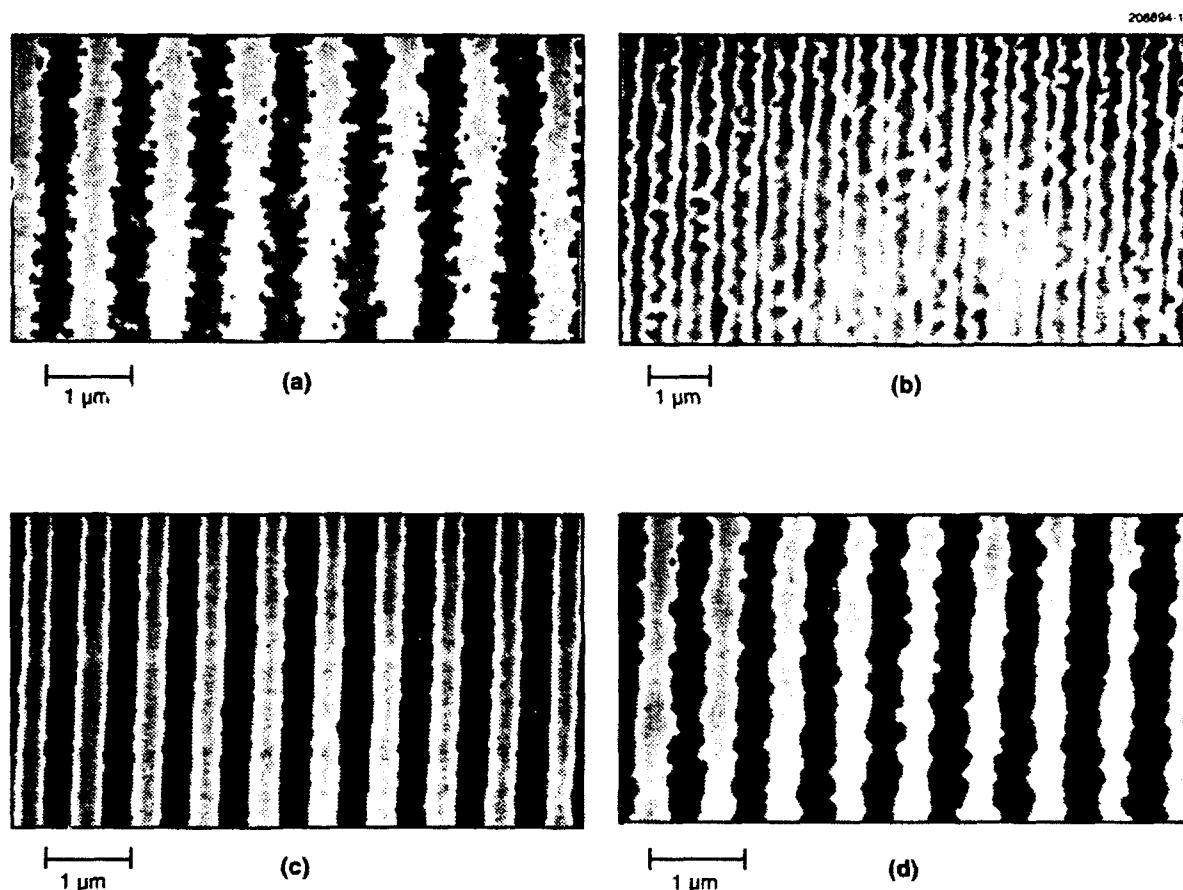
Figure 4-2. Scanning electron micrographs of grating patterns printed using various resist formulations: (a) poly[(methyl silyne)-co-(isobutyl silyne)] (60/40), (b) poly[(n-propyl silyne)-co-(cyclohexyl silyne)] (70/30), (c) poly[(n-butyl silyne)-co-(isobutyl silyne)] (80/20), and (d) poly[(n-propyl silyne)-co-trimethylsilyl] (90/10).

31
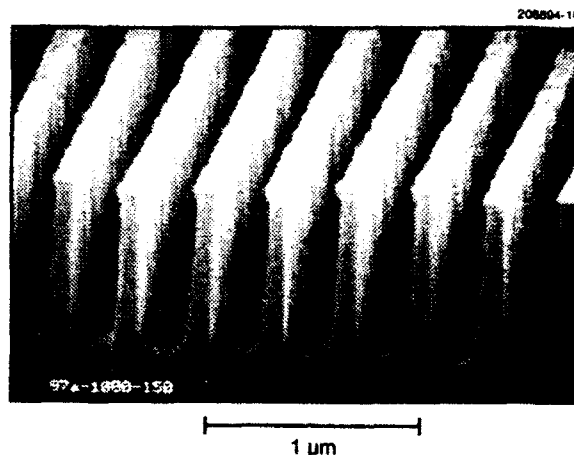
Figure 4-3. Pattern with 0.2-μm lines and spaces printed in 30-nm-thick poly(n-butyl silyne) on 1-μm-thick hard-baked polymer resin, using an exposure dose of 50 mJ/cm². Oxygen reactive ion etching was used to transfer the pattern into this planarizing layer.

in molecular weight via copolymerization with 40-mol% poly(isobutyl silyne); note the large line-edge roughness (~ 200 nm). Likewise, other resist formulations show varying degrees of line-edge roughness, as indicated by Figures 4-2(b) through 4-2(d). Figure 4-3, which shows 0.2-μm features printed using poly(n-butyl silyne), exhibits some line-edge roughness, but it is only about 20 nm in magnitude. The source of the line-edge roughness is not shot noise, since the exposure conditions result in $>10^6$ photons per pixel. Atomic force imaging of the resist surfaces indicates a short-range surface roughness of only 1.4 nm (1σ), well below the magnitude of the line-edge roughness observed in Figure 4-2(a). We attribute the increased roughness in Figure 4-2(a) to the existence of microgel phases that cannot be filtered. These microgel phases are present when the solubility parameter of the polymer is low as in the case of methyl silyne copolymer systems.

The development latitude for ±10% linewidth control was also measured. A value of roughly 100% was obtained, with an optimal development time of 20 ± 10 s observed. This latitude was measured for a 0.4-μm feature ($k_1 = 0.46$), and is limited by incomplete dissolution at short development times and relatively minor swelling at long times.

R. R. Kunz   D. A. Smith*

M. W. Horn   J. R. Eshelman*

P. A. Bianconi*

32

4.2 MODELING OF POSITIVE-TONE SILYLATION PROCESSES FOR 193-nm LITHOGRAPHY

Silylation, the selective incorporation of silicon into polymer films, will render the polymer resistant to plasma etching and can be used to implement high-resolution surface-imaging resist systems. Single-component resists, with a pure novolac or polyvinylphenol resin, will crosslink when exposed at 193 nm using an argon fluoride excimer laser. This surface crosslinking forms a template that impedes the diffusion of the silylating agent into the exposed areas of the film, and a positive-tone image results after plasma development [8]. The depth and profile of silylation affect the resolution, feature size control, and process latitude of these resist systems.

We conducted a series of experiments to develop and evaluate a process model for positive-tone silylation. All the experiments used polyvinylphenol resin silylated with dimethylsilyldimethylamine. The silylation was carried out between 80 and 100°C, at 10 Torr, for times between 1 and 3 min. Resist exposures were performed using an attenuated beam directly from a laser for open-frame exposures, or using a prototype exposure tool with a 5×-reduction, 0.22-NA catadioptric lens with a partial coherence of 0.68 [7]. Fourier transform infrared spectroscopy was employed to monitor the extent of silylation. The Si-O-phenyl peak at ~ 910 wave numbers was used to follow the reaction. Cross-sectional staining of the silylated profiles was carried out by exposing the edge of cleaved samples to an oxygen reactive ion etching plasma.

Our initial silylation process model involved two steps: computing the aerial image using a commercial optics modeling program and convolving this image with the silylation characteristic function. The silylation characteristic was determined by exposing resist samples in the open-frame mode at varying doses and measuring the silylation depth and etch resistance. This procedure was performed for 1-min silylations at 80 and 100°C, which resulted in silylation depths of 75 and 180 nm, respectively, in unexposed films. Milder silylation conditions require less exposure to cause enough crosslinking to impede silylation. The doses required to print open-frame exposures for the 80 and 100°C silylations were 25 and 50 mJ/cm^2, respectively.

Figure 4-4 illustrates the predicted silylation profile based on the measured silylation behavior and the calculated aerial image for a 0.5-μm line-and-space grating exposed with 2.5 times the open-frame exposure dose. A large discrepancy is evident when the predicted profile is compared to a profile taken from micrographs of plasma-stained samples. The predicted profile is much wider and shows a tapered appearance, while the actual profile is much narrower, slightly shallower, and more rounded. This general trend can be observed in the series of micrographs shown in Figure 4-5. The figure shows silylation profiles for a set of gratings with feature sizes in the range 0.8–0.3 μm. While the largest features show the tapered profile predicted from the model, the smaller features show a generally rounded shape. All the micrographs are at the same magnification, so it can also be seen that the depth of silylation decreases as the feature size becomes smaller. This general trend would be predicted by the degradation of the aerial image for smaller features, but the measured silylation depth is consistently less than would be calculated based solely on the aerial image degradation.
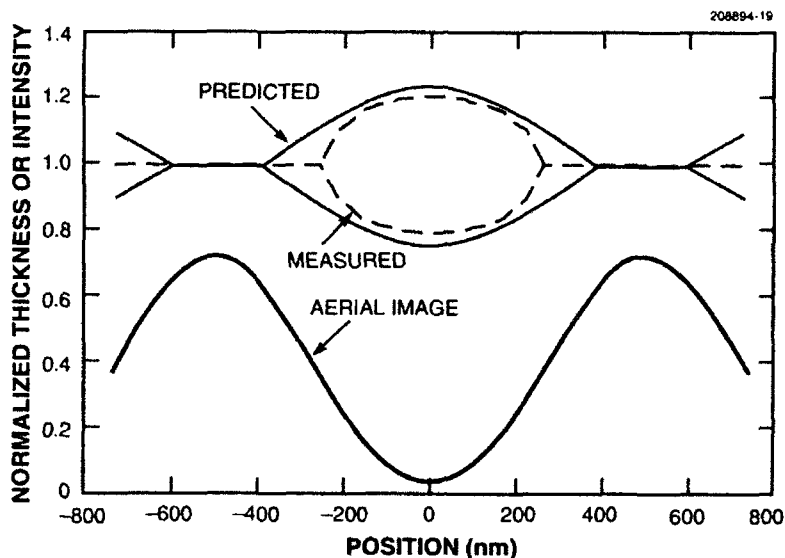
33

Figure 4-4. Comparison of theoretical and experimental silylation profiles for a 0.5-μm line-and-space grating pattern. The aerial image is also shown, corresponding to $k_1 = 0.57$ and a modulation transfer function of 0.89.

Another factor that can influence the depth of silylation is the nature of the diffusion process for the silylating agent in the resist film. Several previous studies [9]–[11], as well as work with the 193-nm positive-tone process [12], have confirmed that silylation occurs by a Case II diffusion mechanism. In contrast to Fickian diffusion, a Case II diffusion process indicates that the relative rates for diffusion and polymer relaxation are comparable [13]. This is a well-known [14] phenomenon for diffusion of organic species into polymer films, as is the case during the silylation process. In models for Case II diffusion, the rate of diffusion into the film is governed by the swelling associated with the reagent incorporation. This swelling creates a stress mismatch between the swollen silylated layer and the unsilylated resist [13]. The micrographs in Figure 4-5 clearly show that there is less swelling for the smaller feature sizes. Since the crosslinked areas of the film hinder the diffusion of silylating agent and do not swell, they impose a constraint on the swelling that occurs in the adjacent unexposed areas. As these boundary constraints move closer together for the smaller features, less swelling can occur, and thus the rate of silylation is further reduced.

A similar argument holds for the variation in silylation that occurs as a function of feature type. The amount of silylation for the isolated line is smaller than that for the lines in the grating structure. Additionally, the isolated spaces are well under their nominal sizes, since the swelling of the adjacent

34

areas has encroached on the exposed portion of the film. In the comparison between the isolated lines and the gratings, the aerial images are very similar, so the model does not predict any significant difference in silylation profile. However, the amount of crosslinking adjacent to the silylated region is much greater for the isolated line, and this would tend to impose a greater constraint on the amount of swelling that can occur. For the isolated space, the lack of any exposed areas adjacent to it allows those regions of the film to swell fully. This swelling causes additional stress on the exposed area so the amount of silylation tends to be greater than would be predicted from the aerial image.
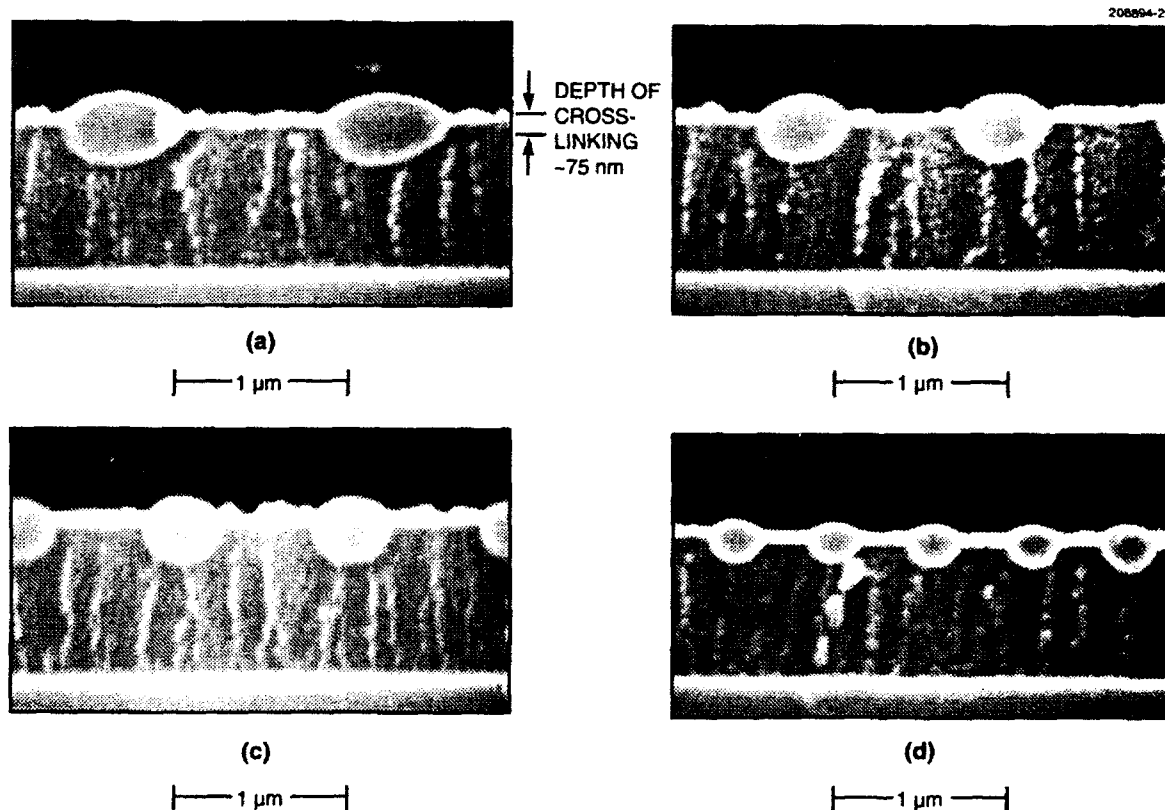

Figure 4-5. Scanning electron micrographs of plasma-stained silylation profiles of line-and-space patterns for features (a) 0.8, (b) 0.6, (c) 0.5, and (d) 0.3 μm.
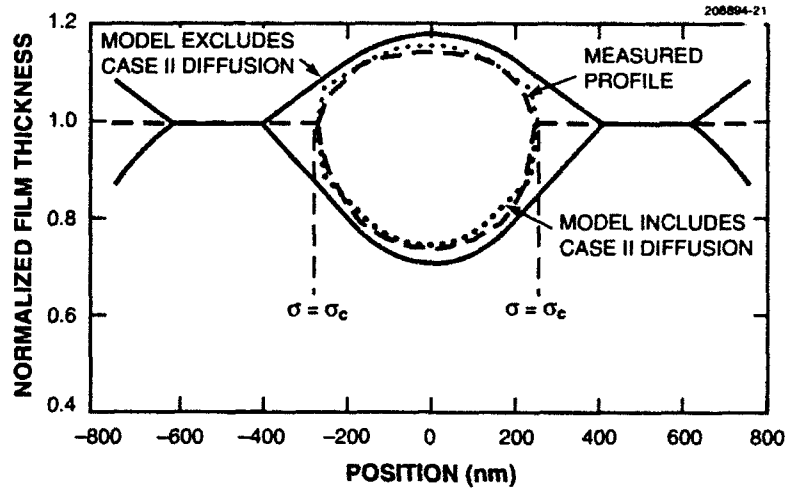
Figure 4-6. Comparison of theoretical and experimental silylation profiles for a 0.5-μm line-and-space grating pattern. The dotted curve includes the effects of Case II diffusion and the solid curve neglects these effects. The dashed curve illustrates the profile measured with a scanning electron microscope.

One theoretical treatment of Case II diffusion relates the swelling front velocity (or in this case the silylation rate) to the extent to which the swelling stress exceeds the critical stress for crazing [15]. This approach leads to a three-parameter equation containing an Arrhenius expression with a parameter K, the critical swelling stress σ_c, and an activation energy E_a:

$$dv / dx = K\left(\sigma - \sigma_c\right)\exp\left(-E_a / kT\right) . \tag{4.1}$$

It is apparent from Figure 4-4 that whereas our initial model predicts a small amount of swelling at the edge of the features, none occurs since the critical swelling stress has not been exceeded. The model can be improved by including the Case II diffusion effects, which will require determining σ_c and K. We have assumed that the critical swelling stress is attained at the edge of the experimentally observed profile, as shown in Figure 4-6. The swelling is proportional to the silylation depth (40% of the total thickness), which is in turn proportional to the dose. Thus, the critical stress occurs at a fixed dose, and the amount of silylation in this revised model is determined by the difference between the exposure dose and this critical swelling dose. The factor K is then determined by matching the thickness of the silylated region in the center of the feature. With these two parameters the depth of silylation is then recalculated, based on the aerial image and the critical stress model, and is in much better agreement with the experimental data, as indicated in Figure 4-6.

M. A. Hartney

REFERENCES

1. D. C. Hofer, R. D. Miller, and C. G. Wilson, *Proc. SPIE* **469**, 16 (1984).

2. R. R. Kunz, P. A. Bianconi, M. W. Horn, R. R. Paladugu, D. C. Shaver, D. A. Smith, and C. A. Freed, *Proc. SPIE* **1466**, 218 (1991).

3. R. R. Kunz, M. W. Horn, R. B. Goodman, P. A. Bianconi, D. A. Smith, J. R. Eshelman, G. M. Wallraff, R. D. Miller, and E. J. Ginsberg, *Proc. SPIE* **1672**, 385 (1992).

4. R. C. Weast (ed.), *CRC Handbook of Chemistry and Physics*, 62nd ed. (CRC, St. Louis, 1981), p. C-699.

5. G. M. Wallraff, R. D. Miller, N. Clecak, and M. Baier, *Proc. SPIE* **1466**, 211 (1991).

6. D. A. Smith and P. A. Bianconi, presented at Int. Symp. Silicon Polymers, Los Angeles, Calif., 3–4 April 1992.

7. D. C. Shaver, D. M. Craig, and C. Marchi, *Proc. SPIE* **1674**, 766 (1992).

8 M. A. Hartney, R. R. Kunz, D. J. Ehrlich, and D. C. Shaver, *Proc. SPIE* **1262**, 119 (1990).

9. R. J. Visser, J. P. W. Schellekens, M. E. Reuhman-Huisken, and L. J. van Ijzendoorn, *Proc. SPIE* **71**, 111 (1987).

10. E. K. Pavelchek, J. F. Bohland, J. W. Thackeray, G. W. Orsula, S. K. Jones, B. W. Dudley, S. M. Bobbio, and P. W. Freeman, *J. Vac. Sci. Technol. B* **8**, 1497 (1990).

11. B. A. Chen, T. P. Ma, A. C. Spencer, and W. Cunningham, Jr., *Proc. Mid-Hudson Section Soc. Plastics Engineers. Photopolymers: Principles, Processes, and Materials* (Society of Plastics Engineers, Brookfield, Conn., 1985), p. 169.

12. M. A. Hartney, M. Rothschild, R. R. Kunz, D. J. Ehrlich, and D. C. Shaver, *J. Vac. Sci. Technol. B* **8**, 1476 (1990).

13. N. L. Thomas and A. H. Windle, *Polymer* **529**, 23 (1982).

14. J. Crank and G. S. Park, *Diffusion in Polymers* (Academic, New York, 1968).

15. C. Gostoli and G. C. Sarti, *Polymer Eng. Sci.* **22**, 1018 (1982).

5. HIGH SPEED ELECTRONICS

5.1 SCANNING TUNNELING MICROSCOPY OF FIELD-EMISSION CATHODES

The realization of RF power tubes having significantly improved efficiency demands that traditional heated thermionic cathodes be replaced by novel cathode structures that emit electrons at room temperature via field emission. The use of such field-emission cathodes in traveling-wave tubes is projected to improve the power-added efficiency by 10–20%. In addition, semiconductor microfabrication technology now enables extremely small vacuum microtriodes to be built, in which the cathode-anode and cathode-grid spacings are < 1 μm. The use of thermionic cathodes in these devices is impractical, both because the heat from the cathodes can degrade the nearby electrodes and because the emission current density from thermionic cathodes is too low to enable useful operation of these devices in the microwave range.

We are now using a scanning tunneling microscope (STM) to evaluate the emission properties of candidate materials for field-emission cathodes. A schematic cross section of our STM is shown in Figure 5-1. In one measurement mode, the tip in this instrument can be precisely scanned over a sample within a few angstroms of the surface to detect and image the emission from individual atoms. Figure 5-2 shows an STM image of a graphite surface that was taken in this mode as part of a qualification test for our STM. This figure clearly demonstrates the atomic-resolution capability of the instrument. In an alternative measurement mode, the instrument tip can be scanned over the sample at a larger tip-sample distance of tens or hundreds of angstroms to characterize the average emission over the cathode surface. It is this mode that we are using for our cathode studies.

Figure 5-3(a) shows a scanning electron micrograph of a field-emission cathode comprising an array of molybdenum knife edges fabricated on a silicon substrate, and Figure 5-3(b) presents an STM image of the emission from the same array. The emission is quite uniform along each knife edge in this sample. The slight differences in shape between the knife edges and their emission profiles are due to roughness of the STM scanning tip as well as its finite radius of ~ 10 nm.

To enable rapid evaluation of the emission from a variety of cathode materials, we have recently installed the STM in an ultrahigh-vacuum evaporator as shown in Figure 5-4. In this arrangement the sample faces two electron-beam guns that are used to evaporate fresh coatings of different materials onto the knife edges. The degree of emission, the emission uniformity, and the work function of each material are assessed using the STM as shown in the inset. The gas inlet in the evaporator enables gases such as oxygen to be introduced onto the cathode surfaces to determine the effects of contamination on the emission.

<div align="right">

C. O. Bozler
S. Rabe

</div>

208894-22

TIP VIEWING

SAMPLE HOLDER

SAMPLE

TIP

X-Y-Z PIEZOELECTRIC SCANNER

INCHWORM MOTOR

VIBRATION ISOLATION SUPPORT

METAL-GASKET-SEALED FLANGE
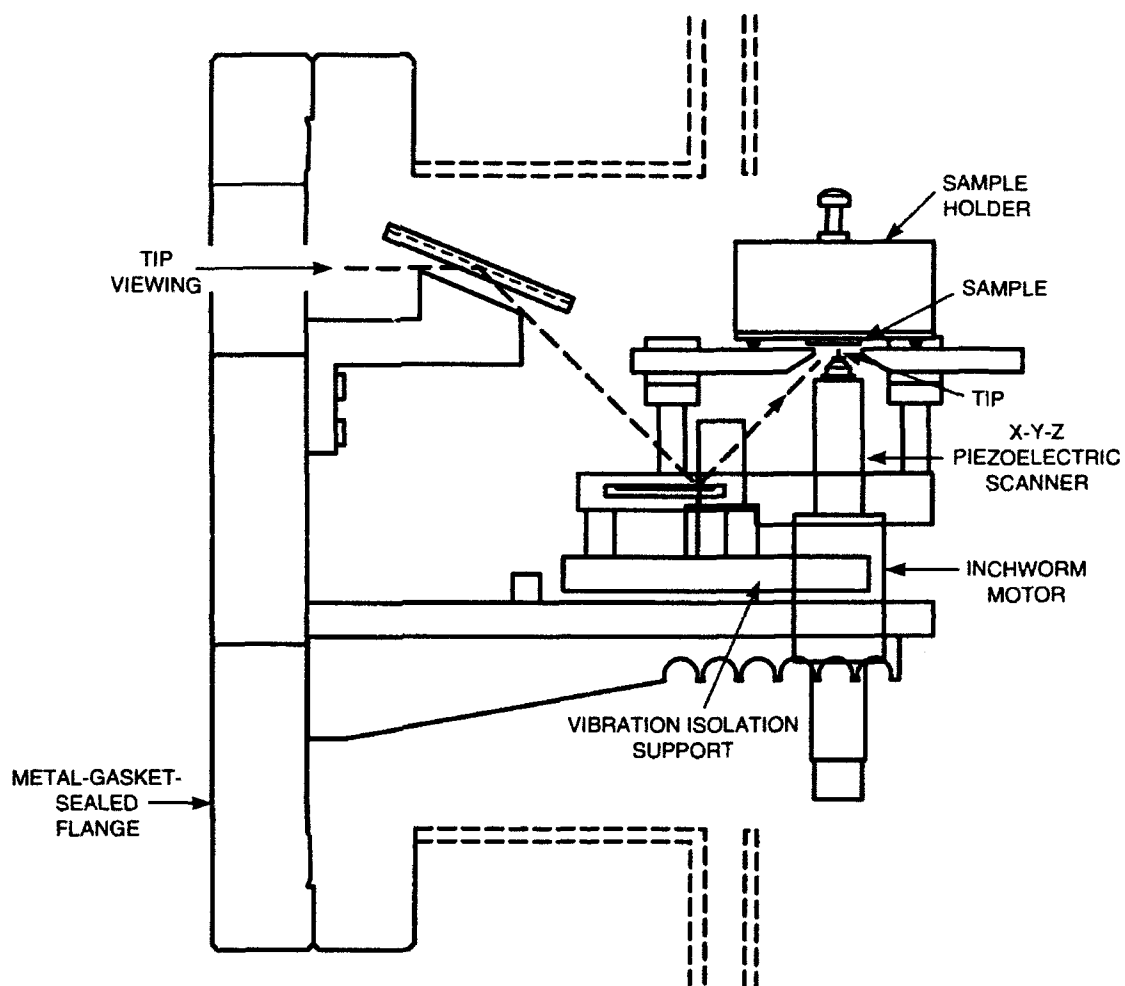
Figure 5-1. Schematic cross section of a scanning tunneling microscope (STM).

40
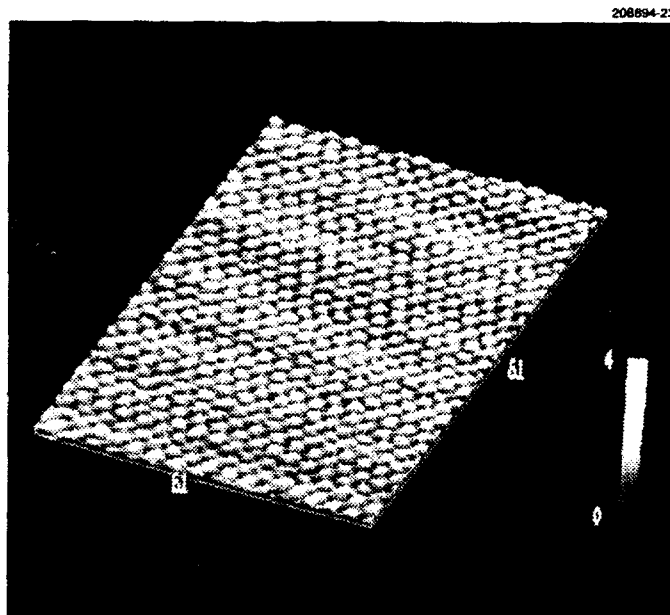
Figure 5-2. STM image of a graphite surface. Each bright hillock represents one carbon atom.

41

208894-24

(a)
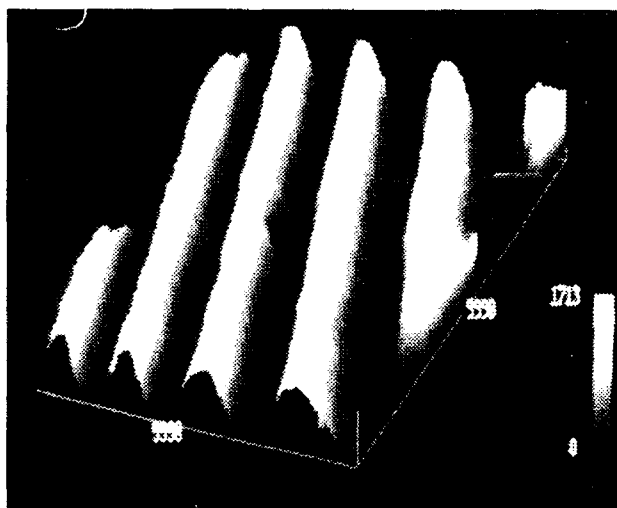
(b)

Figure 5-3. (a) Scanning electron micrograph and (b) STM image of a field-emission cathode comprising an array of molybdenum knife edges fabricated on a silicon substrate. The periodicity of the array is 0.32 μm.

208694-26

SAMPLE UNDER TEST

STM HEAD
WITH HOT
STAGE

THICKNESS AND RATE
MONITOR

GAS INLET

PUMP

ELECTRON-BEAM EVAPORATORS

FIELD-EMITTER ARRAY

ELECTRON
EMISSION

STM SAMPLING TIP

Figure 5-4. Schematic of the ultrahigh-vacuum evaporator with STM installed.

43

6. MICROELECTRONICS

6.1 1024 × 1024 FRAME-TRANSFER CCD IMAGER

In previous reports we have described a 420 × 420-pixel frame-transfer charge-coupled device (CCD) imager [1]. This device has been used in multichip arrays for low-light-level visible-band imaging and for soft x-ray spectroscopic imaging [2], and it also has provided a vehicle for much of our work on back illumination [3] and radiation hardening [4],[5]. However, a larger version of the device is desirable for the above applications where a broad field of view demands large 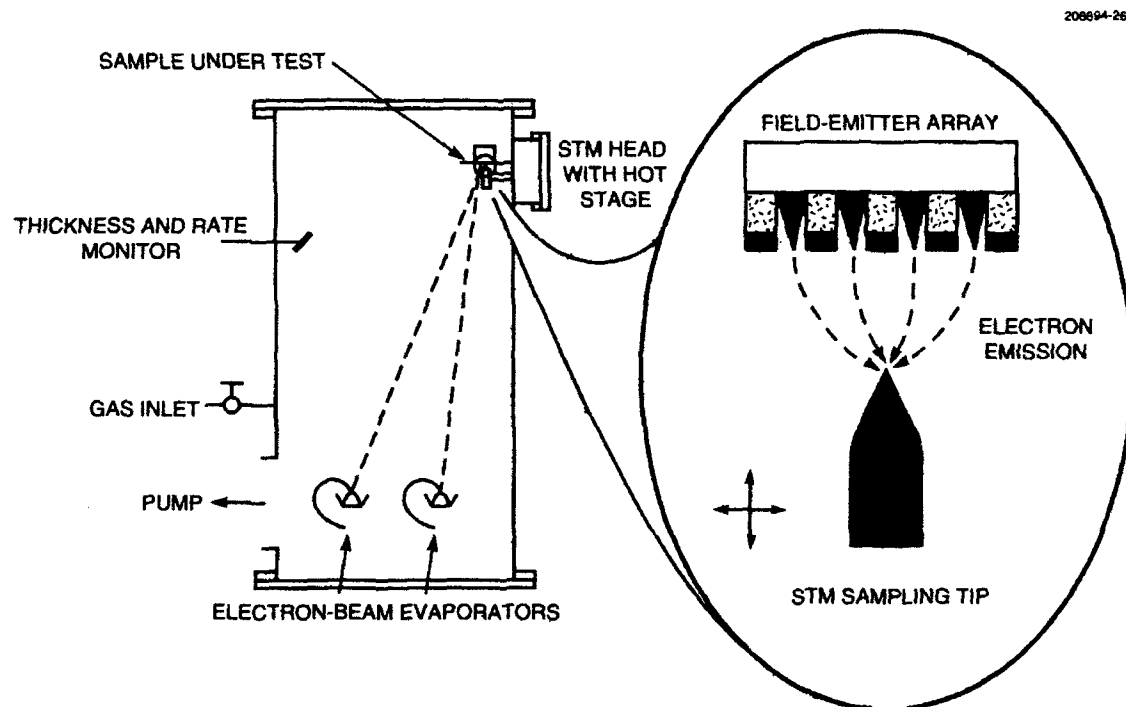focal-plane coverage but with a minimum number of chips. The high yields on recent lots of the 420 × 420 device indicate that our processing technology can readily support a much larger chip. Here, we describe a new 1024 × 1024-pixel device and some initial test results.

The new imager is depicted schematically in Figure 6-1 and resembles in many respects the smaller imager. As was the case with the 420 × 420-pixel device, this imager is fabricated with the three-phase, triple-polysilicon n-buried-channel process and is designed to allow close abutting to other imagers on three sides of the imaging array. However, the pixel sizes are somewhat smaller than previously, being 24 × 24 μm in the imaging section, and 13.5 × 21 μm along the vertical and horizontal dimensions, respectively, in the nontapered portions of the frame store. Also, for this device the minimum gap between adjacent chips on the left and right sides is ~ 30 μm larger because clock lines run along both sides of the imaging array, as opposed to a single side in the smaller chip. Driving the imaging array gates from both ends reduces the rise time for charging the polysilicon gates by 4 times compared to single-ended excitation. This rise time limits the transfer rate from imaging array to frame store, and with a single set of clock lines the transfer time would have been unacceptably long.

Another requirement for this device was that it have noise performance comparable to that of the smaller chip at a 5-Hz frame rate. Since the new device has almost 6 times more pixels, the output data rate would likewise be 6 times greater for the same frame rate. This higher rate would degrade the noise performance as well as necessitate a redesign of the output circuit to increase its bandwidth. The solution to this problem that avoided a redesign was to use four output ports. This was done by separating the frame store into two halves, each containing 512 columns. The output register for each frame store has an output circuit at both ends, for a total of four ports. Each output register can be clocked entirely to either the left or right (for two-port operation) or with each half of the register clocked toward the respective outputs (for four-port operation).

This device is currently being fabricated on 100-mm wafers, in contrast to the 3-in.-diam wafers used for the smaller imager. In spite of the larger area, only four chips can fit on the wafer because of the very large die size (25 × 40 mm). For a device of this size, yield is of great concern. For the first lot, ~ 80% of the devices were free of basic defects such as gate gate and gate-substrate shorts. This is somewhat better than the yields projected from the smaller device and indicates that much larger devices, perhaps as large as an entire 100-mm wafer, are feasible. Figure 6-2 shows a photograph of the new device in a 72-pin package (right) and, for comparison, the 420 × 420 device in a 44-pin package (left).

208894-27

IMAGING ARRAY
1024 (H) × 1026 (V) PIXELS
24 × 24 μm

P1 O—
P2 O—
P3 O—

—O P1
—O P2
—O P3

FRAME STORE AB
512 (H) × 1026 (V)
21 (H) × 13.5 (V) μm

O P1
O P2
O P3

FRAME STORE CD
512 (H) × 1026 (V)

P1 O—
P2 O—
P3 O—

OUT A   B C   D

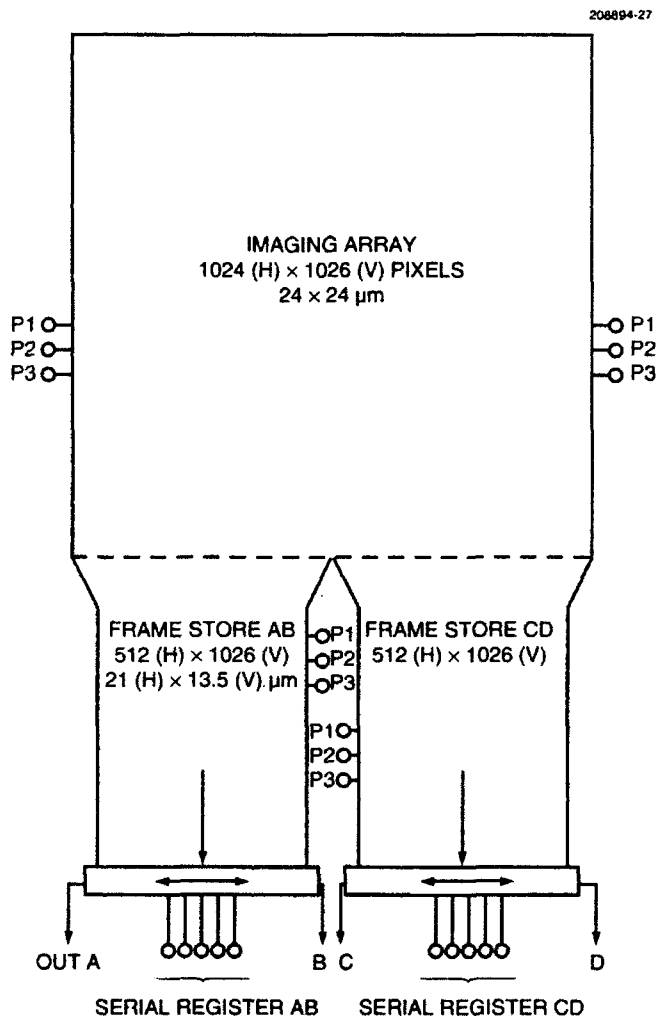SERIAL REGISTER AB   SERIAL REGISTER CD

Figure 6-1. Schematic representation of the 1024 × 1024-pixel frame-transfer CCD imager. The imaging and frame store areas each have two additional rows of pixels to allow for misalignment of a light shield and other design-related factors.

46

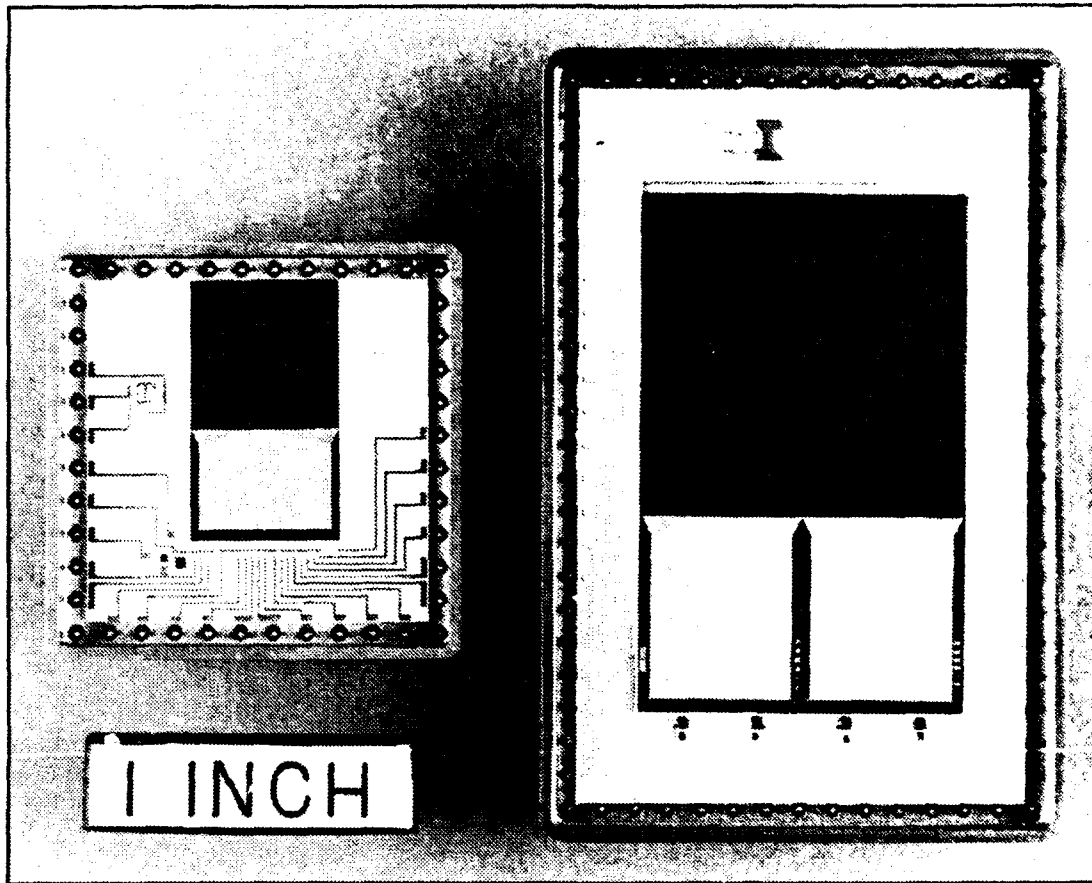*Figure 6-2.* *Photograph of the new 1024 × 1024-pixel imager in a 72-pin package (right) and the older 420 × 420-pixel device in a 44-pin package (left). Additional chip components inside the packages include buffer amplifiers and temperature sensors.*

Preliminary testing of this device has confirmed the basic operating modes and revealed no design flaws.

B. E. Burke
R. W. Mountain
D. J. Young

6.2 VARIATION OF CHARGE-TRANSFER INEFFICIENCY WITH CHARGE PACKET SIZE IN PROTON-IRRADIATED CCDs

In space-based applications of CCD imagers, bulk traps can be created in the buried channel by naturally occurring high-energy proton bombardment. These traps lead to an increase in the charge-transfer inefficiency (CTI) of the device, which can be improved by a modified buried-channel profile [5]. This special profile consists of an additional buried-channel implant in the form of a narrow potential trough that confines charge packets to a smaller volume and thereby reduces contact between the packets and the electron traps.

This report describes measurements of CTI on proton-irradiated CCD devices for charge packets of varying sizes. The measurements were performed on a 420×420 CCD, containing a trough, that had been subjected to 5.5×10^{10} protons/cm^2 with an energy of 40 MeV. The procedure for measuring the CTI consisted of clearing all pixels at the temperature of interest (either -75 or -115°C) and then uniformly illuminating the device so that it appeared as shown schematically in Figure 6-3(a), where a darker tone represents more electrons in a pixel. The frame store region was then cleared of charge, and several seconds were allowed to pass so that traps in the frame store region could empty, as shown in Figure 6-3(b). The charge in the imaging array was clocked through the frame store region, as shown in Figure 6-3(c), and all 420 pixels in each row were then read out and summed off chip. During clocking through the frame store region, the first one or two rows lose some electrons to the empty traps in the frame store. The amount of charge per row is illustrated in Figure 6-3(d), where the upper rows still contain the original Q_0 charges per pixel, while the charge for the first row is diminished by the quantity Q_{loss}. The procedure was then repeated using a different time of illumination to obtain different values for Q_0.

Q_{loss} measurements are converted to CTI of a parallel transfer in the frame store, and the CTI is plotted against the size of the charge packet in Figure 6-4. The upper and lower curves represent measurements made at -75 and -115°C, respectively. (The two square data points indicate the CTI of this device as measured previously using an Fe[55] x-ray source that produces packets of 1620 electrons.) It is apparent, at either temperature, that the CTI is worst for packets less than 100 electrons. It is preferable to operate devices at -115°C, which was previously shown to be the optimum temperature for operation of irradiated CCDs made of similar material using 1620-electron packets [6]. The curves go through minima around 3×10^4 electrons and local maxima near 7×10^4 electrons. Two-dimensional solutions of Poisson's equation, using the CANDE program, support the hypothesis that the increase in CTI beyond 3×10^4 electrons is due to charge overfilling the trough and spilling over into the full width of the channel, exposing the electrons in the packet to more traps. With further increases in charge packet size, the CTI reaches a maximum and then decreases again.

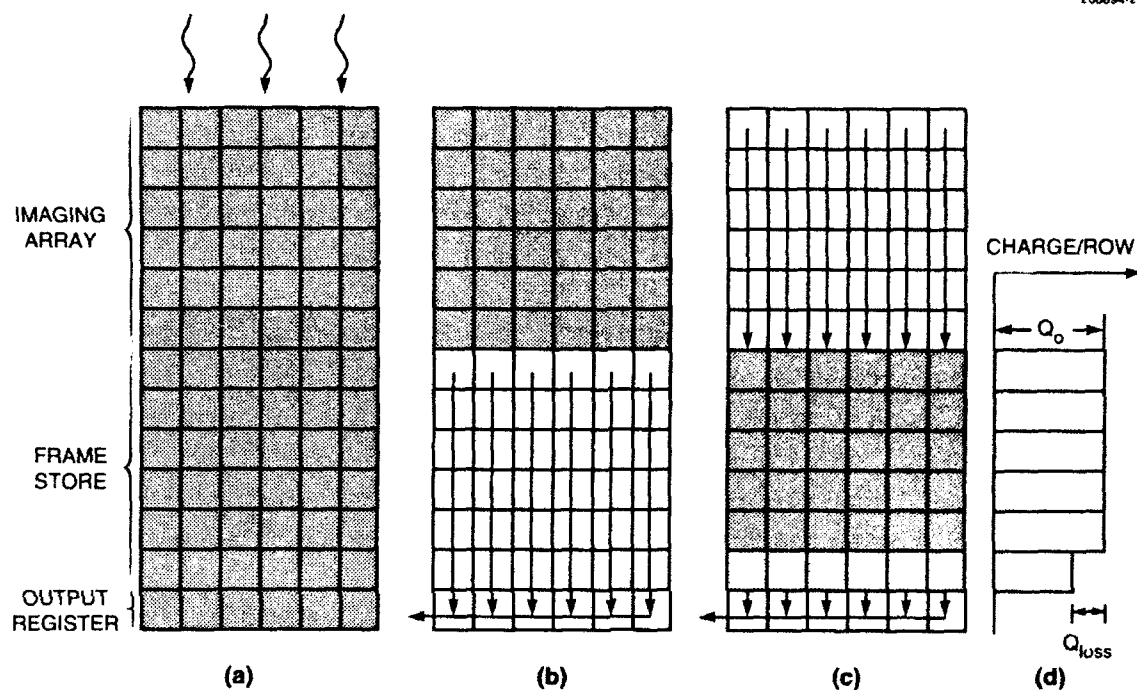J. A. Gregory
B. E. Burke
M. J. Cooper

48

Figure 6-3. Schematic representation of procedure for measuring charge-transfer inefficiency (CTI) of a CCD containing proton-bombardment-induced traps: (a) flat field illumination of imaging array and frame store, (b) clocking out of charge in frame store, (c) clocking of filled pixels from imaging array through frame store, and (d) charge distribution in rows after readout and summation.
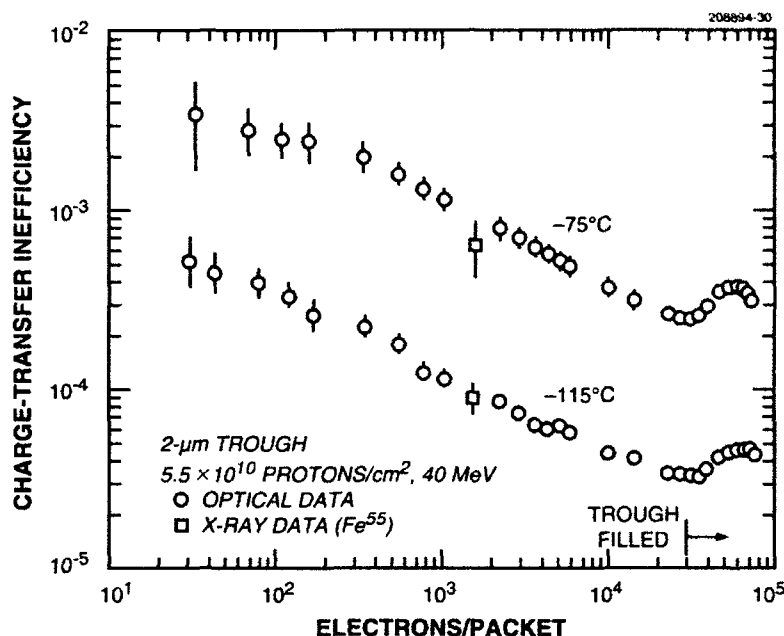
Figure 6-4. Dependence of CTI on electrons/packet in a proton-bombarded CCD. Data were acquired at −75 and −115°C. The two square data points indicate the CTI of the device as measured previously using an Fe⁵⁵ x- ay source that produces packets of 1620 electrons.

The figure shows a plot with CHARGE-TRANSFER INEFFICIENCY on the y-axis (from 10^{-5} to 10^{-2}) and ELECTRONS/PACKET on the x-axis (from 10^1 to 10^5). Labels include: 2-µm TROUGH, 5.5×10^{10} PROTONS/cm^2, 40 MeV, O OPTICAL DATA, □ X-RAY DATA (Fe^{55}), −75°C, −115°C, TROUGH FILLED.

REFERENCES

1. Solid State Research Report, Lincoln Laboratory, MIT, 1988:3, p. 61.

2. B. E. Burke, R. W. Mountain, D. C. Harrison, M. W. Bautz, J. P. Doty, G. R. Ricker, and P. J. Daniels, *IEEE Trans. Electron Devices* **38**, 1069 (1991).

3. Solid State Research Report, Lincoln Laboratory, MIT, 1989:4, p. 61.

4. Solid State Research Report, Lincoln Laboratory, MIT, 1990:2, p. 51.

5. Solid State Research Report, Lincoln Laboratory, MIT, 1990:4, p. 61.

6. Solid State Research Report, Lincoln Laboratory, MIT 1991:3, p. 39.

7. ANALOG DEVICE TECHNOLOGY

7.1 MEASUREMENT AND MODELING OF NONLINEAR EFFECTS IN STRIPLINES

Our measurements and analysis showing that the surface impedance Z_s in $YBa_2Cu_3O_{7-x}$ (YBCO) is a function of the RF magnetic field H_{rf} have been reported previously [1],[2]. Here, we report a complete characterization of the nonlinear effects in high-quality thin films of YBCO by determining $Z_s = R_s + iX_s$ as a function of frequency f, temperature T, and RF magnetic field, where R_s is the surface resistance, $X_s = \mu_0\omega\lambda$, μ_0 is the permeability of free space, ω is the angular frequency $2\pi f$, and λ is the penetration depth.

Nonlinear effects are of interest as a means of understanding the loss mechanisms in the high-T_c materials. These materials have been marked by a large residual surface resistance, which has not yet been satisfactorily explained. It is hoped that better understanding of the nonlinear effects will also lead to better understanding of both the residual values and other sources of loss, such as from flux penetration in the mixed state.

In addition, the nonlinear effects can be used as a diagnostic tool for the material. A potential source of nonlinearities is Josephson-junction weak links that result from large-angle grain boundaries or possibly from inclusions of other phases or nonstoichiometric material. Changes in the growth conditions, e.g., a higher deposition temperature, can sometimes eliminate such nonidealities. It may be that determination of the nonlinear RF surface impedance is one of the most sensitive methods to detect these and other defects in the films.

The basic measurement method, which is based on a stripline resonator, has been described in detail previously [3],[4]. The films used are grown epitaxially on $LaAlO_3$ by off-axis in-situ sputtering [5]. These very high quality films have a low-field surface resistance comparable to that of other high-quality films grown by alternative methods [6],[7].

We divide the evaluation of nonlinear effects into two parts, X_s vs H_{rf} and R_s vs H_{rf}. To determine $X_s = \mu_0\omega\lambda$, we measure the shift in resonant frequency Δf as the input power is increased. Using Δf and the calculation of the inductance per unit length of the stripline as a function of λ, we can calculate the change in λ as a function of H_{rf} [2]. To determine $R_s(H_{rf})$ we measure the resonator Q vs input power. Then R_s is calculated from the Q.

Typical curves for $\Delta f/f$ vs RF current and R_s vs H_{rf} are shown in Figures 7-1 and 7-2, respectively. The results were obtained at 77 K for a resonator made of material with $T_c = 86.4$ K and operating at its fundamental resonance of 1.5 GHz. Figure 7-1 also illustrates a fit to the data derived from an exact calculation of $\Delta f/f$ using Ginzburg-Landau theory as discussed in [8]. Compared to changes in R_s, the changes in λ ($\Delta\lambda/\lambda < 10^{-3}$) and therefore in the inductance of the stripline were small. Because of the small changes in λ, we have used the low-power current distribution in the analysis of the nonlinear R_s results that follow.
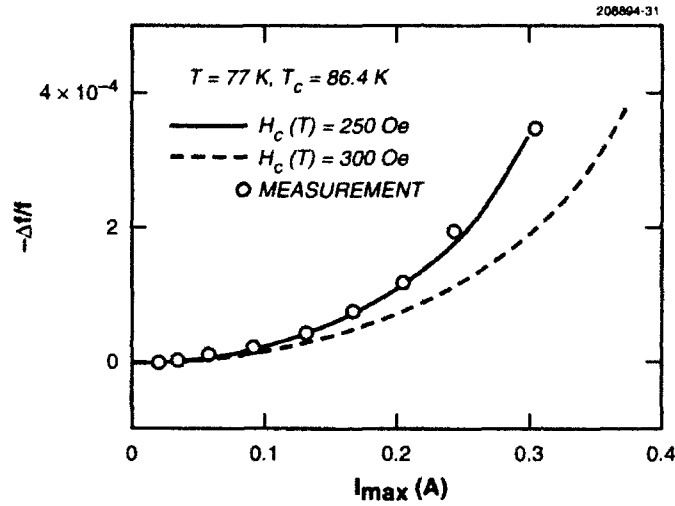
51

Figure 7-1. Shift in resonant frequency vs RF current. The solid line was calculated numerically using the exact Ginzburg-Landau solution for the stripline geometry with $H_c = 250$ Oe. The dotted line used $H_c' = 300$ Oe and illustrates the sensitivity of the calculation to H_c.
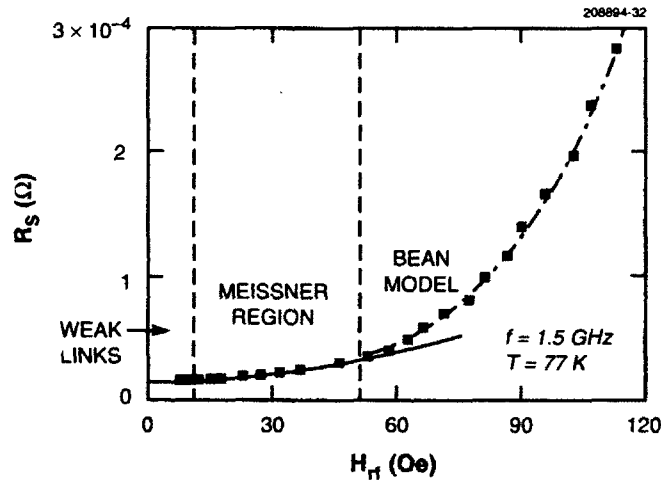

Figure 7-2. Typical R_s vs H_{rf} curve, here for $T = 77$ K and $f = 1.5$ GHz. The graph is divided into three regions of H_{rf} that we used to model the results: low-field weak links, intermediate-field Meissner region, and high-field Bean model. The solid line is a fit of $R_s{}^M = a + b\,(f, T)\,H_{rf}{}^2$ to the results in the Meissner region, and the dot-dashed line is a fit that takes into account flux penetration.
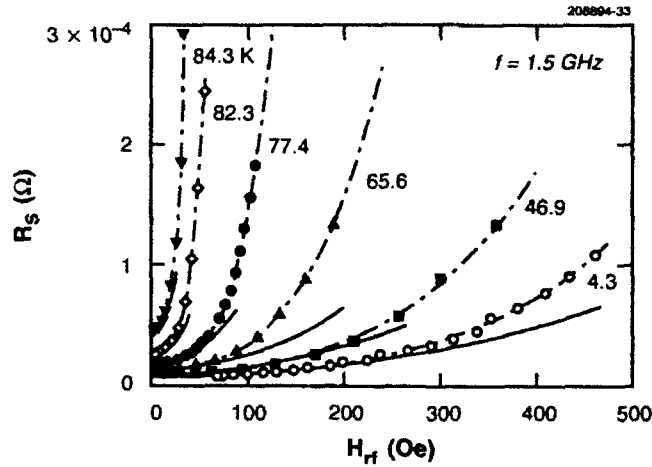
Figure 7-3. Selected R_s vs H_{rf} results for f = 1.5 GHz with temperature as a parameter. The fits are the same as in Figure 7-2.
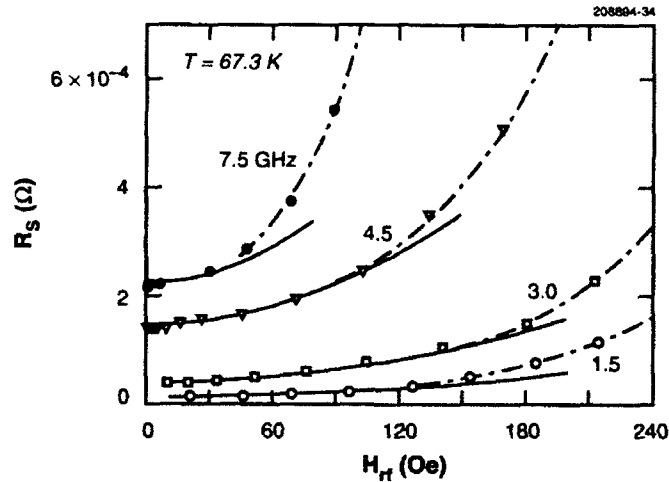

Figure 7-4. Selected R_s vs H_{rf} results for T = 67.3 K with frequency as a parameter. The fits are the same as in Figure 7-2.

Figures 7-3 and 7-4 show the temperature and frequency dependences of R_s vs H_{rf}, respectively, for the same resonator as in Figures 7-1 and 7-2. Two other resonators from films of very similar quality have shown behavior qualitatively the same as in these figures. The conclusions that we draw about the loss mechanisms are the same for all of the resonators we have examined. Figure 7-2 illustrates the model used to fit our results for $R_s(H_{rf})$.

53

At low field ($H_{rf} < 10$ Oe), R_s vs H_{rf} shows very small scale structure, which is not visible in Figure 7-2. This structure probably results from weak links [9]. We focus here on the technologically interesting behavior at higher fields. Our results can best be explained by dividing them into (1) the Meissner (intermediate-field) region and (2) the mixed-state (high-field) region, which are separated at a field that we define as H_{c1}^{rf} (~ 50 Oe in Figure 7-2), where the onset of flux penetration becomes observable. In the Meissner region the surface resistance follows the functional form $R_s^M = a + b(f,T)H_{rf}^2$, where a and b are fitting parameters. The solid line in Figure 7-2 is a fit of this form to the data in the Meissner region. The fit is consistent with that estimated from time-independent Ginzburg-Landau theory [10].

Figure 7-2 shows a significant deviation from the H_{rf}^2 dependence (solid line) for $H_{rf} > 50$ Oe, which leads us to propose flux penetration as the explanation. When the maximum field at the edge of a current-carrying line exceeds H_{c1}, vortices begin to appear. This means the current distribution is determined by the London penetration depth in the Meissner state and by the Bean critical state model [11] in the mixed state. In the Bean critical state model the extra losses due to flux penetration result from hysteresis. Using this model, Norris [12] calculates the hysteresis loss per cycle per unit length, L_c, for an isolated thin strip carrying a dc current and obtains

$$L_c(F) = I_c^2 \frac{\mu_0}{\pi} \left[(1-F)\ln(1-F) + (1+F)\ln(1+F) - F^2 \right] , \tag{7.1}$$

where $F = I_{rf}/I_c$ and $I_c = J_c A$, with I_{rf} being the RF current, J_c the dc critical current density, and A the cross-sectional area of the strip.

Using the Norris result [12] to generate an approximate expression for the effective surface resistance for hysteresis losses resulting from flux penetration, we obtain $R_s^B = f G(T) L_c (I_{rf}/I_c)$, where $G(T)$ is a geometric factor. In the region where $H_{rf} > H_{c1}^{rf}$, the total effective surface resistance is given by the sum of the Meissner expression and the hysteresis expression, $R_s = R_s^M + R_s^B$. At sufficiently large H_{rf}, R_s^B dominates over R_s^M. In Figure 7-2 the dot-dashed line, obtained by adjusting G and J_c, is a fit that takes into account flux penetration.

With this model of the $R_s(f,T,H_{rf})$, we can discuss the curves of Figures 7-3 and 7-4. Figure 7-3 shows R_s vs H_{rf} at 1.5 GHz with temperature as a parameter, and Figure 7-4 shows R_s vs H_{rf} at a fixed temperature, $T = 67.3$ K, with frequency as a parameter. In principle, data could be obtained at higher frequencies, but only those modes shown had sufficient signal-to-noise ratio to be measured. In order to obtain better data at higher frequencies, resonators with stronger coupling must be used. This option is being investigated. The fitting procedures for the curves of Figures 7-3 and 7-4 were identical to those used for Figure 7-2.

In the high-field region, the frequency dependence of the surface resistance changes from $R_s \propto f^2$, which holds for the intermediate-field region, over to $R_s \propto f$. This is most clearly indicated in the curves of Q vs RF current for the first two modes of the resonator, shown in Figure 7-5. At low field the Q is approximately proportional to $1/f$, as one would expect for $R_s \propto f^2$ because $Q \propto f/R_s$. As the power is increased the Q curves merge, and at high power the Q is independent of frequency, which is a strong indication that R_s is now proportional to f. Since losses proportional to frequency are typical of hysteresis, we propose that the losses found at high power are dominated by hysteresis.

15 × 10³

T = 77 K
○ f = 1.5 GHz
● f = 3.0 GHz

RESONATOR Q
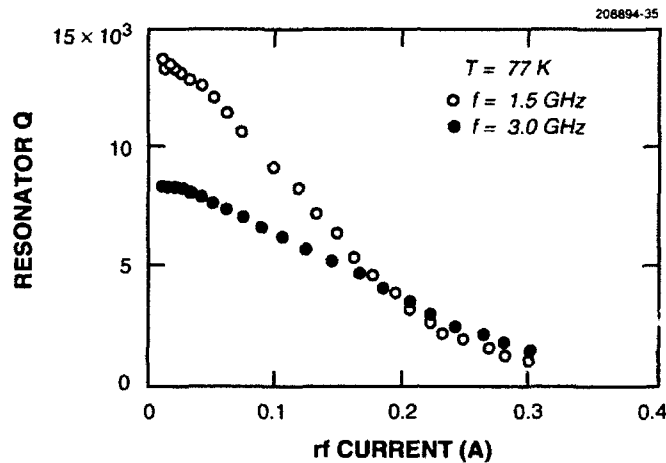
10

5

0

0   0.1   0.2   0.3   0.4

rf CURRENT (A)

Figure 7-5. Q vs RF current for the first two modes of the resonator at T = 77 K. The curves merge at high current, showing that the frequency dependences of Q and therefore R_s change at high power.

It remains unknown whether the power dependences deduced from our measurements are an intrinsic property of the material. This question is very important for applications of these materials in microwave-frequency passive devices, such as resonators and filters, in which lower nonlinearities would be desirable. If the power dependences are not intrinsic to the material, then efforts undertaken by the material fabricators should improve them. We have previously observed [3] larger dependences than those reported here, so we know that variations are possible.

D. E. Oates   M. S. Dresselhaus[†]
P. Nguyen*
G. Dresselhaus*

*Rome Laboratory, Hanscom AFB, Massachusetts.

[†]Department of Electrical Engineering and Computer Science and Department of Physics, Massachusetts Institute of Technology, Cambridge, Massachusetts.

REFERENCES

1. Solid State Research Report, Lincoln Laboratory, MIT, 1991:4, p. 67.

2. D. E. Oates, A. C. Anderson, D. M. Sheen, and S. M. Ali, *IEEE Trans. Microwave Theory Tech.* **39**, 1522 (1991).

3. D. E. Oates and A. C. Anderson, *IEEE Trans. Magn.* **27**, 867 (1991).

4. D. E. Oates, A. C. Anderson, and P. M. Mankiewich, *J. Superconduct.* **3**, 251 (1990).

5. A. C. Westerheim, L. S. Yu-Jahnes, and A. C. Anderson, *IEEE Trans. Magn.* **27**, 1001 (1991).

6. H. Piel, to be published in *Proc. 4th Int. Symp. on Superconductivity (ISS'91)* (Springer, Tokyo).

7. H. Piel and G. Müller, *IEEE Trans. Magn.* **27**, 854 (1991).

8. C-W. Lam, D. M. Sheen, S. M. Ali, and D. E. Oates, *IEEE Trans. Appl. Superconduct.* **2**, 58 (1992).

9. J. Halbritter, *J. Appl. Phys.* **68**, 6315 (1990); **71**, 339 (1992).

10. T. VanDuzer and C. W. Turner, *Principles of Superconductive Devices and Circuits* (Elsevier, New York, 1981).

11. T. P. Orlando and K. A. Delin, *Foundations of Applied Superconductivity* (Addison-Welsey, Reading, Mass., 1991).

12. W. T. Norris, *J. Phys. D* **3**, 489 (1970).

REPORT DOCUMENTATION PAGE

Public reporting burden for this collection of information is estimated to average 1 hour per response, including the time for reviewing instructions, searching existing data sources, gathering and maintaining the data needed and completing and reviewing the collection of information. Send comments regarding this burden estimate or any other aspect of this collection of information, including suggestions for reducing this burden to Washington Headquarters Services, Directorate for Information Operations and Reports, 1215 Jefferson Davis Highway, Suite 1204, Arlington, VA 22202-4302, and to the Office of Management and Budget, Paperwork Reduction Project (0704-0188), Washington, DC 20503.

1. AGENCY USE ONLY (Leave blank)	2. REPORT DATE 15 August 1992	3. REPORT TYPE AND DATES COVERED Quarterly Technical Report, 1 May – 31 July 1992

4. TITLE AND SUBTITLE

Solid State Research

6. AUTHOR(S)

Alan L. McWhorter

5. FUNDING NUMBERS

C — F19628-90-C-0002
PE — 63250F
PR — 221

7. PERFORMING ORGANIZATION NAME(S) AND ADDRESS(ES)

Lincoln Laboratory, MIT
P.O. Box 73
Lexington, MA 02173-9108

8. PERFORMING ORGANIZATION REPORT NUMBER

1992:3

9. SPONSORING/MONITORING AGENCY NAME(S) AND ADDRESS(ES)

HQ Air Force Material Command
AFMC/STSC
Wright-Patterson AFB, OH 45433-5001

10. SPONSORING/MONITORING AGENCY REPORT NUMBER

ESC-TR-92-149

11. SUPPLEMENTARY NOTES

None

12a. DISTRIBUTION/AVAILABILITY STATEMENT

Approved for public release; distribution is unlimited.

12b. DISTRIBUTION CODE

13. ABSTRACT (Maximum 200 words)

This report covers in detail the research work of the Solid State Division at Lincoln Laboratory for the period 1 May through 31 July 1992. The topics covered are Electrooptical Devices, Quantum Electronics, Materials Research, Submicrometer Technology, High Speed Electronics, Microelectronics, and Analog Device Technology. Funding is provided primarily by the Air Force, with additional support provided by the Army, DARPA, Navy, SDIO, NASA, and DOE.

14. SUBJECT TERMS

electrooptical devices	high speed electronics	laser arrays	ultraviolet lithography
quantum electronics	microelectronics	photorefractive effects	field-emission cathodes
materials research	analog device technology	strained-layer quantum wells	charge-coupled devices
submicrometer technology	lasers	infrared intersubband absorption	superconductor surface impedance

15. NUMBER OF PAGES
86

16. PRICE CODE

17. SECURITY CLASSIFICATION OF REPORT	18. SECURITY CLASSIFICATION OF THIS PAGE	19. SECURITY CLASSIFICATION OF ABSTRACT	20. LIMITATION OF ABSTRACT
Unclassified	SAR	SAR	SAR